Semaphorin7A patterns neural circuitry in the lateral line of the zebrafish

Agnik Dasgupta[1,*], Caleb C. Reagor[1,2], Sang P. Paik[1,3], Lauren M. Snow[1,4], Adrian Jacobo[1,5], and A. J. Hudspeth[1]

[1] Howard Hughes Medical Institute and Laboratory of Sensory Neuroscience, The Rockefeller University, New York, NY, USA

*Corresponding author: Dr. Agnik Dasgupta
Laboratory of Sensory Neuroscience
The Rockefeller University
New York, NY 10065
Telephone: 212-327-7353
E-mail: adasgupta@rockefeller.edu

[2] Tri-Institutional PhD Program in Computational Biology and Medicine, New York, NY, USA

[3] Present address: Department of Functional Neuroanatomy, Institute for Anatomy and Cell Biology, Heidelberg University, Heidelberg, Germany

[4] Present address: Brigham and Women's Hospital, Boston, MA, USA

[5]Chan Zuckerberg Biohub San Francisco, San Francisco, CA, USA

Abstract

In a developing nervous system, axonal arbors often undergo complex rearrangements before neural circuits attain their final innervation topology. In the lateral line sensory system of the zebrafish, developing sensory axons reorganize their terminal arborization patterns to establish precise neural microcircuits around the mechanosensory hair cells. However, a quantitative understanding of the changes in the sensory arbor morphology and the regulators behind the microcircuit assembly remain enigmatic. Here, we report that Semaphorin7A (Sema7A) acts as an important mediator of these processes. Utilizing a semi-automated three-dimensional neurite tracing methodology and computational techniques, we have identified and quantitatively analyzed distinct topological features that shape the network in wild-type and Sema7A loss-of-function mutants. In contrast to those of wild-type animals, the sensory axons in Sema7A mutants display aberrant arborizations with disorganized network topology and diminished contacts to hair cells. Moreover, ectopic expression of a secreted form of Sema7A by non-hair cells induces chemotropic guidance of sensory axons. Our findings propose that Sema7A likely functions both as a juxtracrine and as a secreted cue to pattern neural circuitry during sensory organ development.

Introduction

Pathfinding axons are directed to their appropriate synaptic targets by a variety of guidance cues. While approaching or traversing the target field, the growth cones of migrating axons encounter secreted or cell surface-attached ligands and respond by steering toward or away from their sources (1–4). Fine-grained control of these factors is critical for the establishment of proper neural circuitry.

The zebrafish's lateral line provides a tractable *in vivo* system for exploring the mechanisms that guide the assembly of neural circuits in a peripheral nervous system. In particular, it is possible to detect individual hair cells and the sensory axons that innervate them throughout the first week of development (5). The primary posterior lateral line on each side of the zebrafish's tail consists of about seven neuromasts, which contain mechanoreceptive hair

46 cells of opposing polarities—half sensitive to headward (rostrad) water motion and the
47 complementary half to tailward (caudad) water motion—that cluster at their centers (6). The
48 sensory axons of the lateral-line nerve branch, arborize, and consolidate around the basolateral
49 surfaces of the hair cells (Figure 1A). To aid in an animal's swimming behavior, these hair cells
50 sense water currents and relay signals to the brain through the sensory axons (7). The well-
51 defined structure of the ramifications and synaptic contacts of the sensory axons highlight the
52 need to determine the molecular signals behind the assembly of such precise microcircuits (8).
53 We adopted a candidate-gene strategy to seek factors that direct the growth of afferent
54 growth cones in the zebrafish's lateral line. Analysis of single-cell RNA sequencing data
55 identified the *semaphorin7a* (*sema7a*) gene to be highly expressed in hair cells of that organ
56 (9). Semaphorins are important regulators of axonal growth and target finding during the
57 patterning of diverse neural circuits (10). The semaphorin family includes proteins that are
58 secreted, transmembrane, and cell surface-attached (11). Among these, Semaphorin7A
59 (Sema7A) is the only molecule that is anchored to the outer leaflet of the lipid bilayer of the cell
60 membrane by a glycosylphosphatidylinositol (GPI) linker (11). Unlike many other semaphorins,
61 which act as repulsive cues (12,13), Sema7A is involved in promoting axon growth (4) and
62 imparting directional signals by interacting with the integrin and plexin families of receptors
63 residing on the pathfinding axons (14–16). Sema7A likely occurs *in vivo* in both GPI-anchored
64 and soluble forms (17–19), and studies of neuronal explants confirm that both forms can induce
65 directed axonal outgrowth (4). Furthermore, it has been proposed that the GPI anchor is
66 cleaved by membrane-resident GPI-specific phospholipases (GPI-PLs) or matrix
67 metalloproteases to release the Sema7A into the extracellular environment and thus regulate
68 dynamic cellular processes (20,21). Because these observations indicate that Sema7A might
69 influence neuronal development both as a juxtracrine and as a diffusive signal, we investigated
70 the role of Sema7A in sculpting a vertebrate peripheral sensory organ.

71 **Results**

72 **Sema7A expression and localization in hair cells.** The zebrafish genome contains a single
73 *sema7a* gene that produces two transcripts. One transcript encodes Sema7A-GPI, a full-
74 length, GPI-linked, cell surface-attached protein. The second transcript yields Sema7A^{sec}, a
75 protein with a truncated C-terminus, which we conjecture is secreted into the local environment.
76 Each transcript encodes an N-terminal signal sequence and a single copy of the conserved
77 Sema domain (11). To detect the presence of both *sema7a* transcripts in the hair cells of the
78 lateral-line neuromasts, we used fluorescence-activated cell sorting (FACS) to capture the
79 labeled hair cells (22) and isolated total RNA. Using primers that flank the regions encoding
80 the conserved Sema domain and the distinct C-termini of the two transcripts, we performed
81 reverse transcription and polymerase chain reactions (RT-PCR) to identify both the membrane-
82 anchored and the secreted transcript in developing larvae (Figure 1B-D; Figure 1—figure
83 supplement 1A-D). Single-cell RNA sequencing data also have shown that the GPI-linked
84 *sema7a* transcript is particularly enriched in the immature and mature hair cells of the
85 neuromast during early larval development (9), a period when sensory axons of the posterior
86 lateral line contact hair cells and form synapses with them (5,23). Indeed, we have observed
87 Sema7A to be specifically localized in both mature and immature hair cells (Figure 1E; Figure
88 1—figure supplement 2A-D).

89 As neuromasts mature, the contacts between sensory axons and hair cells increase in
90 number, become stabilized, and establish synapses (5,23). Because Sema7A can modulate
91 axon guidance (4,14) and synapse formation (15), we wondered whether the level of Sema7A
92 also changes during neuromast development. Upon quantifying the average intensity of
93 Sema7A, we found similar expression in rostrally and caudally polarized hair cells of
94 neuromasts at 1.5, 2, 3, and 4 days post fertilization (dpf). The average Sema7A intensity
95 increased significantly over this period in both rostrally and caudally polarized hair cells. At
96 1.5 dpf, the neuromasts harbor primarily immature hair cells that make minimal contacts with
97 sensory axons and do not form stable association with axonal terminals (23). At this stage the
98 average Sema7A intensity in hair cells remained low. By 2-4 dpf the hair cells mature to form

99 stable contacts and well-defined synapses with the sensory axons (5,24). The average
100 Sema7A intensity in hair cells at each of these stages rose to levels that significantly exceeded
101 those of 1.5 dpf neuromasts (Figure 1F). This rise in the amount of Sema7A during neuromast
102 maturation supports a role for Sema7A in the guidance of sensory axons and their interaction
103 with hair cells.

104 We additionally demonstrated an anisotropic distribution of Sema7A along the
105 apicobasal axis of each hair cell. As neuromasts develop through 2, 3, and 4 dpf, Sema7A
106 remained highly enriched in the subapical region of the hair cell, the site of the Golgi network
107 (Figure 1E; Figure 1—figure supplement 2E). This localization suggests that Sema7A—like
108 other proteins of the semaphorin family (25)—is directed to the plasmalemma through Golgi-
109 mediated vesicular trafficking. Using the transgenic line *Tg(cldnb:LY-mScarlet)* that expresses
110 membrane-tethered mScarlet in all cells of the neuromast (26), we detected Sema7A at the
111 plasma membrane and potentially in vesicles (Figure 1—figure supplement 2F-I). While
112 Sema7A maintained a high level in the subapical region, the protein increasingly accumulated
113 at the base of the hair cell: the Sema7A level at the hair cell base was low at 2 dpf, but
114 increased sharply by 3 dpf and 4 dpf (Figure 1G; Figure 1—figure supplement 2J). During this
115 period the hair cells increase in number and mature, whereas the associated sensory axons
116 arborize to contact multiple hair cells and form robust synaptic boutons at their bases (5,24).
117 Does progressive basal accumulation of Sema7A facilitate association of sensory axon
118 terminals to the hair cell? To address this question, we utilized doubly labeled transgenic fish
119 *Tg(myo6b:actb1-EGFP;neurod1:tdTomato)* that marked the hair cells and the sensory axons
120 of the posterior lateral line with distinct fluorophores (Figure 1A) (27). We quantified the average
121 Sema7A intensity and the accumulation of sensory arbors, measured by td-Tomato intensity,
122 at the bases of the hair cells. Across developmental stages, the basal association of the
123 sensory arbors showed a positive correlation with Sema7A accumulation (Figure 1H,I;
124 Figure 1—figure supplement 3A-E, Video 1). The progressive enrichment of Sema7A at the
125 hair cell base with the sensory axons suggests that Sema7A acts as a mediator of contacts
126 between sensory axons and hair cells.

127 **Sema7A restricts sensory axons around clustered hair cells**. If Sema7A guides and
128 restricts the sensory arbors at and around the hair cells clustered in a neuromast, then
129 inactivating Sema7A function should disrupt this process. To test this hypothesis, we obtained
130 a *sema7a* mutant allele (*sema7a*^{sa24691}) with a point mutation that introduces a premature stop
131 codon in the conserved sema domain (Figure 2—figure supplement 1A). The homozygous
132 mutant, hereafter designated *sema7a*$^{-/-}$, should lack both the secreted and the membrane-
133 attached forms of Sema7A. The average intensity of Sema7A immunolabeling in hair cells
134 diminished by 61% in *sema7a*$^{-/-}$ larvae (0.34 ± 0.01 arbitrary units) in comparison to controls
135 (0.87 ± 0.01 arbitrary units). In a few cases we observed minute accumulations of Sema7A at
136 the subapical region, but little or no protein at the base of the mutant hair cells (Figure 2A-E).
137 We quantified the number of hair cells in the neuromasts of the control and the *sema7a*$^{-/-}$
138 larvae. We did not observe significant changes in the hair cell number between the genotypes
139 across developmental stages (Figure 2—figure supplement 1B). Furthermore, we tested the
140 mechanotransduction ability of *sema7a*$^{-/-}$ mutant hair cells by labeling with the styryl dye FM
141 4-64 (5). The hair cells of the 4 dpf *sema7a*$^{-/-}$ larvae incorporated the FM 4-64 as effectively as
142 the age-matched control animals. We quantified the FM 4-64 intensities from 60 hair cells and
143 six neuromasts from three control larvae, and from 60 hair cells and six neuromasts from three
144 *sema7a*$^{-/-}$ mutant larvae. The average intensities of FM 4-64 labeling between the genotypes
145 did not show a significant difference, which suggests that the mutation does not impact
146 essential hair cell functions (Figure 2—figure supplement 1C,D; Videos 2,3).

147 To characterize the impact of the *sema7a*$^{-/-}$ mutation on arbor patterning, we utilized
148 doubly labeled transgenic fish *Tg(myo6b:actb1-EGFP;neurod1:tdTomato)* that distinctly
149 labeled the hair cells and the sensory arbors (27). In control neuromasts, the sensory axons
150 approached, arborized, and consolidated around the bases of clustered hair cells (Figure 2F).
151 Although the sensory axons approached the hair cells of *sema7a*$^{-/-}$ neuromasts, they displayed
152 aberrant arborization patterns with wayward projections that extended transversely to the organ
153 (Figure 2G). To quantitatively analyze the arborization morphology, we traced the sensory
154 arbors in three dimensions to generate skeletonized network traces that depict–as

155 pseudocolored trajectories–the increase in arbor length from the point of arborization
156 (Figure 2H, I).

157 To visualize the hair cell clusters and associated arborization networks from multiple
158 neuromasts, we aligned images of hair cell clusters, registered them at their hair bundles, from
159 neuromasts at 2 dpf, 3 dpf, and 4 dpf (Figure 2—figure supplement 1E,F). Throughout
160 development, the arborization networks of control neuromasts largely remained within the
161 contours of the hair cell clusters; the few that reached farther nonetheless lingered nearby
162 (Figure 2J; Figure 2—figure supplement 1G,I). This result suggests that an attractive cue
163 retained the axons near the sensory organ. In *sema7a*$^{-/-}$ neuromasts, however the neuronal
164 arbors failed to consolidate within the boundaries of hair cell clusters and extended far beyond
165 them (Figure 2K; Figure 2—figure supplement 1H,J; Video 4).

166 We quantified the distribution of the sensory arbors around the center of the combined
167 hair cell clusters. For both the control and the *sema7a*$^{-/-}$ neuromasts, the arbor densities peaked
168 proximal to the boundaries of the hair cell clusters. Beyond the cluster boundaries, in control
169 neuromasts at 2 dpf, 3 dpf, and 4 dpf the arbor densities fell sharply at respectively 31.7 μm,
170 36.6 μm, and 32.7 μm from the center. In *sema7a*$^{-/-}$ neuromasts of the same ages, the sensory
171 arbors extended respectively 38.5 μm, 51.4 μm, and 56.6 μm from the center (Figure 2L;
172 Figure 2—figure supplement 1K,L; Figure 2—figure supplement 2A). Furthermore, we
173 quantified the degree of contact of the sensory arbors to their hair cell clusters in individual
174 neuromasts from both control and *sema7a*$^{-/-}$ mutants. In control neuromasts, the degree of
175 contact was 83 ± 1 % (mean ± SEM) at 2 dpf and 84 ± 1 % at 3 dpf, but significantly increased
176 to 90 ± 1 % at 4 dpf (Figure 2M; Figure 2—figure supplement 2B). This observation indicates
177 that the sensory arbors reinforce their association to the hair cell clusters as neuromasts
178 develop. However, in *sema7a*$^{-/-}$ neuromasts such contact was significantly reduced. Only
179 69 ± 4 % of sensory arbors at 2 dpf were closely associated with the corresponding hair cell
180 clusters, a value that remained at 67 ± 2 % at both 3 dpf and 4 dpf (Figure 2M). These findings
181 signify that, with simultaneous disruption of both signaling modalities of Sema7A, the organ

182 fails to restrict the localization of sensory arbors and has significantly diminished contact with
183 them.

184 **Sema7A patterns the arborization network's topology.** Accurate spatial arrangement of the
185 neuronal projections around hair cells is essential for proper retrieval and transmission of
186 sensory information. Mutations that perturb proper assembly of sensory neuronal microcircuits
187 lead to hearing impairment (28). Quantitative insight into the wiring pattern is therefore essential
188 to identify systematic aberrations in the microcircuit arising from genetic deficits. The three-
189 dimensional skeletonized network traces allowed us to accurately delineate the microcircuit
190 topology across individuals, developmental stages, and genotypes from living animals (Figure
191 2D, E). To quantitatively analyze the arbor network, we defined five topological attributes: (1)
192 nodes, denoted as junctions where arbors branch, converge, or cross; (2) loops, comprising
193 minimal arbor cycles forming topological holes; (3) bare terminals, defined as arbors with free
194 ends; (4) the node degree, calculated as the number of first-neighbor nodes incident to a node;
195 and (5) the arbor curvature, measured as the total curvature of a bare terminal (Figure 3A). We
196 quantified these attributes to accurately determine how the circuit topology is established
197 during maturation of the sensory organ in control larvae and how it is impacted by *sema7a*
198 deficit.

199 To determine how internode connectivity is distributed across networks, we quantified
200 the distribution of node degrees along the relative height of the hair cell cluster across
201 individuals, developmental stages, and genotypes. As for most other real-world networks (29),
202 we observed a highly skewed node-degree distribution: the majority of nodes had low node
203 degrees (three and four) and a small number of nodes—often acting as hubs, like the
204 arborization initiation point—had high node degrees (five to seven). The node degree varied
205 from three to seven in control larvae and three to six in *sema7a*$^{-/-}$ larvae. Across
206 developmental stages and genotypes, the high node degrees primarily occurred at the base
207 (region from 0 % to 10 % of the cluster height) of the hair cell cluster and acted as hubs for
208 the majority of branching events. Low node degrees primarily occurred along the basolateral
209 region (region from 10 % to 60 % of the cluster height) of the hair cell cluster. The apical region

210 (region from 60 % to 100 % of the cluster height) was sparsely populated with low node
211 degrees. The network's hierarchical organization along the organ's axis suggests that arbors
212 receive sensory inputs at multiple levels, allowing the network to carry out robust neural
213 computations. Even though nodes of low degree were most prevalent between genotypes
214 across developmental stages, their distribution along the relative organ axis became
215 significantly different at 4 dpf, with nodes in control larvae localized higher along the axis than
216 in *sema7a*$^{-/-}$ larvae (Figure 3A; Figure 3—figure supplement 1A-C; Table 1). These
217 observations indicate that Sema7A regulates both the spatial organization and node-degree
218 complexity of the sensory arbor network.

219 An average of 9.3 sensory axonal branches approach the hair cell cluster of a neuromast
220 (8). Pathfinding of sensory axons around the hair cell cluster results in the formation of axonal
221 fascicles that form numerous loops and bare terminals, which determine the microcircuit
222 topology (Figure 2B, D) (8). To optimally surround and contact the hair cell cluster, do the
223 sensory arbors prefer to adopt one topological feature over the other? To address this
224 question, we measured the correlation between the number of bare terminals and the number
225 of loops across individuals, developmental stages, and genotypes. In both 2 dpf and 3 dpf
226 larvae, the distributions remained highly scattered across individuals and genotypes.
227 However, by 4 dpf in the control larvae the arbor network contained either a high number of
228 loops with a low number of bare terminals or a high number of bare terminals with a low
229 number of loops. This result suggests that the stereotypical circuit topology observed in the
230 mature organ may emerge through transition of individual arbors from forming bare terminals
231 to forming closed loops encircling topological holes. That we did not observe a similar
232 transition in *sema7a*$^{-/-}$ neuromasts of the same age suggests that Sema7A may direct the
233 switch between these two distinct topological features (Figure 3B; Figure 3—figure
234 supplement 1D, E; Table 1).

235 Measurement of the contour length of both bare terminals and loops additionally
236 revealed that across developmental stages in control larvae the sensory arbors followed a
237 three-step process to choose the appropriate topological feature: arbors shorter than 10 μm

238 always formed bare terminals; arbors between 10 μm and 30 μm began to switch between
239 features, with arbors longer than 20 μm strongly preferring to form loops; and arbors longer
240 than 30 μm always formed loops. These results imply that the switch between bare terminals
241 and loops is partly dependent on the length of the arbors. However, this characteristic
242 topological preference was significantly perturbed in the *sema7a*$^{-/-}$ larvae across
243 developmental stages, as many of the sensory arbors longer than 30 μm remained as bare
244 terminals (Figure 3C; Figure 3—figure supplement 1F,G; Table 1). Furthermore, in 4 dpf
245 control neuromasts the majority of the loops contained four nodes and utilized 30-40 μm of
246 arbors to form closed cycles. These conserved topological attributes were significantly
247 perturbed in the *sema7a*$^{-/-}$ larvae of same age (Figure 3D, E; Figure 3—figure supplement
248 2A-D; Table 1). These findings indicate that Sema7A tightly monitors the sensory arbor loop
249 formation, including the preferred loop length and number of nodes per loop, to properly
250 surround and contact the hair cell cluster.

251 As observed previously, bare terminals in control neuromasts project transverse to the
252 organ and linger nearby, often curving back to form new loops and contact the hair cell cluster
253 (Figure 2D,F). To analyze the propensity of the bare terminals to curl backward, we measured
254 their total curvatures, defined as the sum of the curvature at each point along the length of an
255 arbor. Henceforth, we address the total curvature as the curvature of a bare terminal. We
256 classified the bare terminals in two categories: high-curvature arbors with curled morphology
257 and curvature greater than $\pi/6$ (30 degrees); and low-curvature arbors with linear morphology
258 and curvature less than π /6. In control neuromasts 44.8 % of arbors had low curvature
259 compared to 56.4 % in *sema7a*$^{-/-}$ neuromasts at 4 dpf. Concomitantly, 55.2 % of arbors had
260 high curvature in control neuromasts compared to 43.6 % in *sema7a*$^{-/-}$ neuromasts at 4 dpf
261 (Figure 3F; Figure 3—figure supplement 2E, F; Table 1). These observations further confirm
262 our hypothesis that a Sema7A-mediated attractive cue is involved in orienting bare neural
263 arbors toward the hair cell cluster to potentially form loops.

264 In summary, we propose that Sema7A mediates four key aspects of the topology of the
265 arborization network: (1) the node degree complexity along the organ's axis; (2) the transition

266 of arbors from bare terminals to loops; (3) the preference for forming loops containing four
267 nodes with 30-40 μm of arbors; and (4) the preference of bare terminals to adopt higher
268 curvature.

269 **Sema7A^{sec} is a sufficient chemoattractive cue for sensory axon guidance**. Because
270 genetic inactivation of the *sema7a* gene disrupts both signaling modalities of the cognate
271 protein, we could not assess the specific activity of the Sema7A^{sec} diffusive cue in guiding
272 lateral-line sensory axons. To independently verify the potential role of that isoform, we
273 therefore expressed the secreted variant ectopically and investigated the resultant arborization
274 patterns.

275 Analysis of the microcircuit connectivity of the neuromasts has demonstrated bare
276 sensory-axonal terminals in the perisynaptic compartments, where they do not contact the hair
277 cell membrane (8). We speculate that these bare terminals are attracted by a Sema7A^{sec}
278 diffusive cue. To test this hypothesis, we ectopically expressed Sema7A^{sec} protein tagged with
279 the fluorophore mKate2, then analyzed its effect on the morphology of sensory arbors.
280 Fertilized one-cell embryos were injected with the *hsp70:sema7a^{sec}-mKate2* plasmid and
281 raised to 3 dpf. Larvae expressing the transgenesis marker—the lens-specific red fluorescent
282 protein mCherry—were heat-shocked, incubated to allow expression, and subsequently
283 mounted for live imaging. In these larvae, a random mosaic of cells—often embryonic muscle
284 progenitors in the dermomyotome or mature myofibers—expressed the exogenous
285 Sema7A^{sec}-mKate2 protein. We selected only those neuromasts in which a single mosaic
286 ectopic integration had occurred near the network of sensory arbors (Figure 4A,B). In all 22
287 such cases, we observed robust axonal projections from the sensory arbor network toward the
288 ectopically expressing Sema7A^{sec} cells. When the exogenous *sema7a^{sec}* integration occurred
289 in embryonic muscle progenitor cells, which reside in a superficial layer external to the muscle
290 fibers and adjacent to the larval skin (30), the projections were able to form direct contacts with
291 them (Figure 4C; Videos 5,6). But more often, when mature myofibers expressed the
292 exogenous Sema7A^{sec} deep in the myotome, the axonal projections approached those targets
293 but failed to contact them (Figure 4D, Videos 7,8). This behavior likely arose because other

294 components in the myotomal niche—including the fibrous epimysium, other myofibers,
295 myoblasts, and immature myotubes whose surroundings are permeable to diverse diffusive
296 cues (31)—physically obstructed direct interaction of the extended neurites with the ectopically
297 expressing myofibers. All 18 of the injected but not heat-shocked control larvae did not express
298 ectopic Sema7A^{sec}, and we did not observe aberrant projections from the sensory arbor
299 network (Figure 4E).

300 To measure the accuracy of the extended axonal projections in finding the ectopic
301 Sema7A^{sec} source, we defined three parameters: (1) the source path, denoted as the linear
302 distance from the point of arborization to the boundary of an ectopically expressing Sema7A^{sec}
303 cell; (2) the projection path, representing the linear distance from the point of arborization to
304 the terminus of the extended projection; and (3) the projection proximity, calculated as the
305 linear distance from the terminus of the extended axonal projection to the nearest boundary of
306 the ectopically expressing Sema7A^{sec} cell (Figure 4B). We quantified these parameters from
307 18 of the 22 mosaic integration events; in the remainder the extended axonal projections–
308 although following the ectopic source–reentered the posterior lateral-line nerve so that
309 identification of the axon terminals was not possible (Figure 4—figure supplement 1A-A";
310 Video 9). The projection paths of the extended axons reached from 27.1 μm to 142.5 μm while
311 following the ectopic Sema7A^{sec} cues. When we plotted the projection path length against the
312 source-path length, we observed a nearly perfect correlation (Figure 4F). This result signifies
313 that irrespective of the location of the ectopic source–whether proximal or distal to the sensory
314 arbor network–the Sema7A^{sec} cue sufficed to attract axonal terminals from the sensory arbor.
315 Furthermore, the low average projection-proximity length of 3.5 ± 0.7 μm (mean ± SEM)
316 indicated that the extended projection terminals remained either in contact (8 of 18) or in the
317 vicinity (10 of 18) of the ectopic Sema7A^{sec} sources (Figure 4G). These observations together
318 demonstrate that the Sema7A^{sec} diffusive cue is sufficient to provide neural guidance *in vivo*.

319 As the posterior lateral-line ganglion matures, newly formed neurons extend their axonal
320 growth cones along the posterior lateral-line nerve to reach the neuromasts (32). We wondered
321 whether the axonal projections that had yet to be associated with a neuromast could also

respond to an ectopic source of Sema7A^{sec}. Indeed, on seven occasions in which *sema7a^{sec}* integration had occurred between two neuromasts, we detected neurite extensions from the posterior lateral-line nerve to the ectopic Sema7A^{sec} sources (Figure 4H; Figure 4—figure supplement 1B-B", Videos 10-12). Live time-lapse video microscopy further revealed dynamic association between the extending neurites and the ectopic Sema7A^{sec} sources. Long and thin along their entire extents, the neurites were highly motile, extending and retracting rapidly near the Sema7A^{sec} expressing cells. Many neurites maintained their contact with the ectopic sources of Sema7A^{sec} from one hour to almost eight hours (Figure 4I,J; Figure 4—figure supplement 2A, Videos 13-16). The responsiveness of the posterior lateral-line axons to Sema7A^{sec} might therefore be an intrinsic property of the neurons that does not require the neuromast microenvironment.

Sema7A-GPI fails to impart sensory axon guidance from a distance. We speculate that the GPI-anchored transcript variant of the *sema7a* gene can function only through contact-dependent pathways. To test this hypothesis, we expressed the Sema7A-GPI ectopically and investigated the resultant arborization patterns of the sensory axons. Fertilized one-cell embryos were injected with the *hsp70:sema7a-GPI-2A-mCherry* plasmid and raised to 3 dpf. Larvae expressing the transgenesis marker—the lens-specific green fluorescent protein (GFP)—were heat-shocked, incubated to allow expression, and subsequently mounted for live imaging (Figure 5A). In these larvae, a few mature myofibers expressed the exogenous Sema7A-GPI protein. We selected only those neuromasts in which an ectopic integration had occurred near the network of sensory arbors. In all 15 such cases, no sensory axon left the arbor network to approach the ectopic Sema7A-GPI sources. In all 17 of the uninjected and heat-shocked control larvae, the sensory arbor network did not show any perturbation (Figure 5B-C, Videos 17-19). These data suggest that the Sema7A-GPI, unlike its secreted counterpart, functions at the surfaces of the expressing cells.

Sema7A deficiency impacts synaptic assembly. Contact stabilization between an axon and its target cell is essential for synapse formation (33). Neural GPI-anchored proteins can act as

349 regulators of various synaptic-adhesion pathways (34). In the mouse olfactory system, GPI-
350 anchored Sema7A is enriched in olfactory sensory axons and mediates sustained interaction
351 with the dendrites of mitral and tufted cells in the olfactory bulb to establish synapses (15). In
352 the developing mouse brain–particularly in Purkinje cells–GPI-anchored Sema7A instead
353 regulates the elimination of synapses onto climbing fibers (35). The role of anchored Sema7A
354 in regulating synaptic architecture can thus vary according to the cell type and developmental
355 stage. Our demonstration that Sema7A is necessary to consolidate the contact between
356 sensory axons and hair cells during neuromast development suggests a possible role in
357 regulating synaptic structure.

358 Proper synaptogenesis requires the correct spatial organization of the presynaptic and
359 postsynaptic apparatus at the apposition of two cells. At the interface between hair cells and
360 sensory axons, the synaptic network involves two scaffolding proteins in particular: ribeye, a
361 major constituent of the presynaptic ribbons (36), and membrane-associated guanylate kinase
362 (MAGUK), a conserved group of proteins that organize postsynaptic densities (37). Utilizing
363 these scaffolding proteins as markers, we investigated the impact of the *sema7a*$^{-/-}$ mutation on
364 synapse formation. To analyze the distribution of presynaptic densities–immunolabeled with
365 an antibody against the ribeye-associated presynaptic constituent C-terminal binding protein
366 (CTBP) (36)–we counted the number and measured the area of CTBP punctae from multiple
367 neuromasts at several stages of neuromast development (Figure 6A,B). The CTBP punctae in
368 each hair cell ranged from zero to seven across developmental stages. In the zebrafish's
369 posterior lateral line, the formation of presynaptic ribbons is an intrinsic property of the hair cells
370 that does not require contact with lateral-line sensory axons. However, sustained contact with
371 the sensory axon influences the maintenance and stability of ribbons (38). As neuromasts
372 matured from 2 dpf to 4 dpf, we identified similar distribution patterns with a characteristic
373 increase in the number of CTBP punctae in both control and *sema7a*$^{-/-}$ larvae (Figure 6C,D).
374 This result implies that the formation of new presynaptic ribbons is not perturbed in the mutants,
375 even though there are on average fewer CTBP punctae (Figure 6—figure supplement 1A-C).
376 Measurement of the areas of CTBP punctae also showed similar distributions in both

377 genotypes (Figure 6E,F) but the average area of presynaptic densities was reduced in the
378 mutants (Figure 6—figure supplement 1D-F, Figure 6—figure supplement 2). Because GPI-
379 anchored Sema7A lacks a cytosolic domain, it is unlikely that Sema7A signaling directly
380 induces the formation of presynaptic ribbons. We propose that the decrease in average number
381 and area of CTBP punctae likely reflects decreased stability of the presynaptic ribbons owing
382 to lack of contact between the sensory axons and the hair cells.

383 Our analysis of the skeletonized network traces of the sensory arbor network identified
384 distinct topological features that are resultant of collective assemblies of each sensory axon.
385 Because postsynaptic aggregates are organized at the sensory axons, we wondered whether
386 they are associated with a specific topological feature of the network. To identify the distribution
387 of the postsynaptic aggregates along the arbor network, we utilized the transgenic animal
388 *TgBAC(neurod1:EGFP)* that labeled the sensory axons of the posterior lateral line in green
389 fluorescence protein (GFP), and marked the postsynaptic aggregates through immunostaining
390 with a pan-MAGUK antibody (Figure 6G). We generated skeletonized network traces of the
391 arbor network and determined the three-dimensional spatial locations of the MAGUK punctae
392 (Figure 6—figure supplement 2). Comparison of the topological features of the network with
393 the spatial locations of the MAGUK punctae revealed that the postsynaptic densities occur
394 more extensively on the loops than on the bare terminals (Figure 6G). We measured 567
395 MAGUK punctae from 16 sensory arbor networks, where 531 punctae were located on the
396 loops and only 36 punctae on the bare terminals (Figure 6H). Furthermore, the MAGUK
397 punctae predominantly aggregate near the node and their density sharply diminishes moving
398 farther from the node (Figure 6I, Figure 6—figure supplement 2). These observations suggest
399 that the distribution of the postsynaptic aggregates is closely associated with the topological
400 attributes of the sensory circuit. Because in the *sema7a*$^{-/-}$ mutants the arbor networks have
401 significantly lower number of loops and nodes, and more bare terminals, we hypothesize that
402 in the mutants the occurrence of postsynaptic aggregates is perturbed. Moreover, Sema7A-
403 GPI-mediated juxtracrine signaling onto the apposed axonal membrane is essential to induce
404 postsynaptic assembly (15).

405 To characterize the impact of *sema7a* mutation on the formation of postsynaptic
406 aggregates, we counted the number and measured the area of MAGUK punctae from multiple
407 neuromasts at several stages of neuromast development (Figure 6J,K). At 4 dpf, 68.3 % of the
408 hair cells in the control neuromasts were associated with at least one MAGUK punctum. In the
409 *sema7a*$^{-/-}$ mutant this value fell to 37.5 % (Figure 6L,M). The average number of MAGUK
410 punctae also declined in the mutants (Figure 6—figure supplement 1G-I). As control
411 neuromasts matured from 2 dpf to 4 dpf, the MAGUK punctae showed a shift toward smaller
412 sizes, suggesting that the postsynaptic structure fragmented into smaller entities as observed
413 in other excitatory synapses (40). At 4 dpf, 77.5 % of the hair cells in the control neuromasts
414 had postsynaptic densities with areas between 0.10 μm^2 and 0.40 μm^2. In the *sema7a*$^{-/-}$ mutant
415 the corresponding value was only 42.5 % (Figure 6N,O). The average area of MAGUK punctae
416 was also reduced in the mutants compared to the controls (Figure 6—figure supplement 1J-L,
417 Figure 6—figure supplement 2**).** We speculate that the abnormalities in the postsynaptic
418 structure of the *sema7a*$^{-/-}$ mutants arose from reduced contact between the hair cells and the
419 sensory axons and perturbed topological attributes of the sensory circuit or from the lack of
420 Sema7A-GPI-mediated juxtracrine signaling onto the apposed neurite terminals (15).

421 **Discussion**

422 The specification of neural circuitry requires precise control of the guidance cues that direct
423 and restrict neural arbors at their target fields and facilitate synapse formation. In the lateral-
424 line neuromast of the zebrafish, we have identified Sema7A as an essential cue that regulates
425 the interaction between hair cells and sensory axons. We have discovered two isoforms of the
426 *sema7a* gene *in vivo*: the chemoattractive diffusible form is sufficient to guide the sensory
427 arbors toward their target, whereas the membrane-attached form likely participates in sculpting
428 accurate neural circuitry to facilitate contact-mediated formation and maintenance of synapses.
429 Our results suggest a potential mechanism for hair cell innervation in which a local Sema7A^{sec}
430 diffusive cue likely consolidates the sensory arbors at the hair cell cluster and the membrane-
431 anchored Sema7A-GPI molecule guides microcircuit topology and synapse assembly.

432 Establishing the exact function of each of the *sema7a* isoforms will necessitate studies that
433 include transcript-specific targeted mutagenesis and rescue of the *sema7a*$^{-/-}$ mutant phenotype
434 by each of the transcript variants.

435 The role of Sema7A in regulating diverse topological features of the arborization network
436 suggests that microcircuits of control and *sema7a*$^{-/-}$ neuromasts have important functional
437 differences. Loss of Sema7A disrupts the hierarchical organization of the node-degree
438 distribution along the organ's axis, as well as the preference towards forming loops containing
439 four nodes with 30-40 μm of arbors. What benefit does the network gain from surrounding the
440 hair cell cluster with closed loops instead of bare terminals? The network may actively form
441 loops to contribute to the neuromast's overall structure and function, or else emerge as a
442 consequence of the arbors navigating the intervening spaces between the hair cells and
443 support cells. The preferential localization of the postsynaptic aggregates in the loops and an
444 enrichment near the nodes of the arbor network suggest that the precise patterning of the
445 network—with characteristic looping behaviors—is not merely a byproduct of neuromast
446 architecture, but may contribute to the network's ability to gather sensory inputs through
447 properly placed postsynaptic aggregates and to faithfully transmit sensory information to higher
448 processing centers in the hindbrain (7). Further studies are necessary to elucidate the potential
449 role of these topological features in regulating the distribution of synaptic bodies and optimizing
450 robust neural transmission in the lateral-line microcircuit.

451 Recent studies have begun to dissect the molecular mechanisms of semaphorin
452 signaling in axonal navigation. In explants derived from the murine olfactory bulb, Sema7A
453 interacts directly with integrinβ1 to trigger downstream signaling effectors involving focal
454 adhesion kinase and mitogen-activated protein kinases, which are critical regulators of the
455 cytoskeletal network during axonal pathfinding (4,41). Moreover, the interaction between
456 Sema7A and its receptor plexinC1 activates the rac1-cdc42-PAK pathway, which alters the
457 actin network to promote axonal guidance and synapse formation (15,42). We speculate that
458 lateral-line sensory axons utilize similar mechanisms to sense and respond to Sema7A in the
459 establishment of microcircuits with hair cells.

460 During early development of the posterior lateral line, the growth cones of sensory axons
461 intimately associate with the prosensory primordium that deposits neuromasts along the lateral
462 surface of the larva (43,44). The growth of the sensory fibers with the primordium is regulated
463 by diverse neurotrophic factors expressed in the primordium (45,46). Impairing brain-derived
464 or glial cell line-derived neurotrophic factors and their receptors perturbs directed axonal
465 motility and innervation of hair cells (45,46). Lateral-line hair cells are particularly enriched in
466 brain-derived neurotrophic factor (47) and other chemotropic cues (Figure 7). Because the
467 sensory axons of *sema7a*$^{-/-}$ mutants reliably branch from the lateral-line nerve to reach hair cell
468 clusters, these chemoattractive factors might compensate in part for the absence of Sema7A
469 function. Although sensory axons are strict selectors of hair cell polarity and form synapses
470 accordingly (5), diverse chemoattractant cues including Sema7A occur uniformly between hair
471 cell polarities (47). It seems likely that unbiased attractive signals bring sensory arbors toward
472 hair cells, after which polarity-specific molecules on hair cell surfaces dictate the final
473 association between axonal terminal and hair cells. Notch-delta signaling and its downstream
474 effectors regulate hair cell polarity and the innervation pattern (6,8,27). It would be interesting
475 to determine whether Notch-mediated polarity signatures on the hair cell's surface can refine
476 the neuromast neural circuitry.

477 **Materials and Methods**

478 **Zebrafish strains and husband**ry. Experiments were performed on 1.5-4 dpf zebrafish larvae
479 in accordance with the standards of Rockefeller University's Institutional Animal Care and Use
480 Committee. Naturally spawned and fertilized eggs were collected, cleaned, staged, and
481 maintained at 28.5 ºC in system-water with 1 µg/mL methylene blue. Wild-type AB and
482 heterozygous mutant *semaphorin7a*^{sa24691} zebrafish were obtained from the Zebrafish
483 International Resource Center. In addition, the following transgenic zebrafish lines were used:
484 *Tg(myo6b:actb1-EGFP)* (48), *Tg(neurod1:tdTomato)* (27), *Tg(cldnb:LY-mScarlet)* (26), and
485 *TgBAC(neurod1:EGFP)* (39).

486 **Embryo dissociation and flow cytometry**. Immediately before dissection, 4-day-old
487 *Tg(myo6b:actb1-EGFP)* and wild-type larvae were anesthetized in 600 µM 3-aminobenzoic
488 acid ethyl ester methanesulfonate in system water with 1 µg/mL methylene blue. The anterior
489 half of each larva was removed with a fine surgical blade. We used approximately 400 GFP-
490 positive and 50 GFP-negative larvae, the latter for controls of the gating procedure.
491 Dissociation of the tails were performed using a protocol (22) with minor modification; detailed
492 protocol is available upon request. The resuspended cells were incubated for 5 min on ice and
493 sorted with an influx cell sorter (BD Biosciences, San Jose, CA, USA) with an 85 µm nozzle at
494 20 psi and 1X DPBS (Sigma-Aldrich, St Louis, USA). Laser excitation was conducted at
495 561 nm and 488 nm. Distinct populations of GFP-positive hair cells were isolated based on
496 forward scattering, lateral scattering, and the intensity of GFP fluorescence.

497 **RNA extraction and cDNA library preparation**. Sorted cells were collected in a lysis-buffer
498 solution supplemented with β-mercaptoethanol and RNA extraction was performed
499 immediately using a standard protocol (RNeasy Plus Micro Kit; Qiagen). The yield and quality
500 of the product were measured with a bioanalyzer (Agilent 2100). Only samples with an RNA
501 integrity score (RIN) greater than 8.0 were selected for the preparation of cDNA libraries using
502 iScript cDNA Synthesis Kit (BioRad). One nanogram of total RNA was amplified to several
503 micrograms of cDNA.

504 **Reverse transcription-polymerase chain reactions (RT-PCR)**. The *sema7a* gene
505 expresses two transcript variants: variant 1, *sema7a-GPI* anchored, NM_001328508.1; and
506 variant 2, *sema7a*^{sec} secreted, NM_001114885.2. The variant 2 lacks several C-terminal
507 exons, and its 3'-terminal exon extends past a splice site that is used in variant 1. The encoded
508 variant 2 has a shorter and distinct C-terminus than variant 1. To individually identity these
509 transcripts, each of them was PCR amplified from the cDNA library using the following primers:
510 For variant 1, sema7aF= 5´-GGTTTTTCTGAGGCCATTCC-3´, sema7aR1=
511 5´-GGCACTCGTGACAAATGCTA-3´; and for variant 2, sema7aF=
512 5´-GGTTTTTCTGAGGCCATTCC-3´, sema7aR2= 5´-TGTGGAGAAAGTCACAAAGCA-3´. To

513 detect *pvalb8* transcript we used the following primers: pvalb8F=
514 5´-ATGTCTCTCACATCTATCCT-3´ and pvalb8R= 5´-TCAGGACAGCACCATCGCCT-3´. To
515 detect *s100t* transcript we used the following primers: s100tF=
516 5´-ATGCAGCTGATGATCCAGAC-3´ and s100tR= 5´-CTATTTCTTGTCATCCTTCT-3´.

517 **Immunofluorescence microscopy.** For the immunofluorescence labeling of wholemounted
518 wild-type control and *sema7a*$^{-/-}$ larvae, 1.5-4 dpf larvae were fixed overnight at 4 °C in 4 %
519 formaldehyde in phosphate-buffered saline solution (PBS) with 1 % Tween-20 (1 % PBST).
520 Larvae were washed four times with 1 % PBST for 15 min each, then placed for 2 hr in blocking
521 solution containing PBS, 2 % normal donkey serum (NDS), 0.5 % Tween-20, and 1 % BSA.
522 Primary antibodies were diluted in fresh blocking solution and incubated with the specimens
523 overnight at 4 °C. The primary antibodies were goat anti-Sema7A (1:200; AF1835, R&D
524 Systems) (Figure 1—figure supplement 4) (14), rabbit anti-myosin VI (1:200; Proteus 25-6791),
525 murine anti-GM130 (1:200; 610822, BD Transduction Laboratories), murine anti-CTBP (1:200;
526 B-3, SC-55502, Santa Cruz Biotech), and rabbit anti-mCherry (1:200; GTX128508, GeneTex).
527 Larvae were washed four times with 0.1% PBST for 15 min each. Alexa Fluor-conjugated
528 secondary antibodies (Invitrogen, Molecular Probes) applied overnight at 1:200 dilutions in
529 0.2 % PBST included anti-rabbit (488 nm), anti-goat (555 nm), and anti-mouse (647 nm).
530 Larvae were then washed four times in 0.2 % PBST for 15 min each and stored at 4 °C in
531 VectaShield (Vector Laboratories).

532 For the immunofluorescence labeling of postsynaptic density in wholemounted wild-type
533 control and *sema7a*$^{-/-}$ larvae, 2-4 dpf larvae were fixed with 4 % formaldehyde in PBS for
534 4.5-6 hr at 4 °C. Larvae were washed five times with 0.01 % PBST for 5 min each and then
535 rinsed in distilled water for 5 min. The larvae were permeabilized with ice-cold acetone at -20 °C
536 for 5 min. They were rinsed in distilled water for 5 min, washed five times with 0.01 % PBST
537 for 5 min each, and blocked overnight with PBS buffer containing 2 % goat serum and 1 %
538 BSA. Murine anti-pan-MAGUK antibody (1:500; IgG1 NeuroMab, K28.86, 75-029 and
539 MABN72, Millipore) was diluted in PBS containing 1 % BSA, added to the larvae, and incubated
540 for 3 hr at room temperature. Larvae were washed five times for 5 min each with 0.01 % PBST.

541 Alexa Fluor 555-conjugated anti-mouse secondary antibody (1:1000) diluted in PBS containing
542 1 % BSA was added to the larvae and incubated for 2 hr at room temperature. Larvae were
543 washed five times with 0.01 % PBST for 5 min each, rinsed in distilled water for 5 min, and
544 stored at 4 °C in VectaShield (Vector Laboratories).

545 Posterior segments of fixed larvae were mounted on a glass slide and imaged on an
546 Olympus IX81 microscope with a microlens-based, super-resolution confocal microscope
547 (VT-iSIM, VisiTech international) under 60X and 100X, silicone-oil objective lenses of
548 numerical apertures 1.30 and 1.35, respectively. Static images at successive focal depths were
549 captured at 200 nm intervals and deconvolved with the Microvolution software in ImageJ.

550 **Measurement of Sema7A and td-Tomato-positive sensory arbor intensities.** The average
551 Sema7A fluorescence intensities of the hair cells from 1.5 dpf, 2 dpf, 3 dpf, and 4 dpf
552 neuromasts were measured by determining the mean gray level within each hair cell labeled
553 by actin-GFP expression. The intensity distribution of Sema7A protein across the basal cell
554 membrane was measured using the line profile tool in ImageJ (Figure 1—figure
555 supplement 2G-I). The lines were drawn with 1 µm length, starting from the inside of the hair
556 cell to the outside. For each hair cell membrane, the intensity values were scaled from 0 to 1
557 arbitrary units. The intensity distribution of Sema7A protein along the apicobasal axis of the
558 hair cell was measured using the line profile tool in ImageJ (Figure 1—figure supplement 2J).
559 Because hair cell lengths differed among samples, lines were drawn with 2 µm widths and
560 varying lengths of 6-8 µm. For each hair cell, apicobasal length was scaled from 0 to 100
561 arbitrary units and the intensity values from 0 to 1 arbitrary units. The average Sema7A and td-
562 Tomato-positive sensory arbor fluorescence intensities at the hair cell bases from 2 dpf, 3 dpf,
563 and 4 dpf neuromasts were measured by determining the mean gray level within each hair cell
564 basal area, denoted by the region underneath the hair cell nucleus (Figure 1—figure
565 supplement 3A-E).

566 **Genotyping of mutant fish.** The *semaphorin7a*^{sa24691} allele harbors an A-to-T point mutation
567 in the seventh exon of the *semaphorin7a* gene, which creates a premature stop codon (Figure

568 2—figure supplement 1A). Genomic DNA was isolated from the tail fins of adult
569 *semaphorin7a*^{sa24691} (*sema7a*^{sa91}) heterozygous mutant zebrafish. The mutant locus in the
570 genome was PCR amplified using the following primers: sema7a^{sa91}F:
571 5´-AAAGCTGGAAAGCGAATCAA-3´ and sema7a^{sa91}R: 5´-ATATCCAAGGATCCGCCTCT-3´.
572 The 734-base pair amplicons were sequenced, and heterozygous adults were propagated.

573 **Lipophilic styryl fluophore labeling of hair cells.** Freely swimming 4 dpf control and
574 *sema7a*$^{-/-}$ larvae were exposed to the styryl fluorophore FM 4-64
575 (N-(3-triethylammoniumpropyl)-4-(6-(4-(diethylamino) phenyl) hexatrienyl) pyridinium
576 dibromide, ThermoFischer Scientific) at 5 μM for 30 s, then rinsed three times in fresh embryo
577 water and immediately mounted in low-melting-point agarose for live imaging. The average
578 FM 4-64 intensities within the hair cells of 4 dpf neuromasts of both genotypes were measured
579 by determining the mean gray level within each hair cell labeled by actin-GFP expression.

580 **Transient transgenesis with the hsp70l:sema7a^{sec}-mKate2 construct.** The pDNR-LIB
581 plasmid containing the *sema7a*^{sec} coding sequence was purchased from horizon (7140389,
582 Perkin-Elmer). The coding sequence was PCR amplified using the following primers:
583 sema7a^{sec}F:
584 5´-GGGGACAAGTTTGTACAAAAAAGCAGGCTTGATGATTCGACATTATTCT-3´ and
585 sema7a^{sec}R:
586 5´-GGGGACCACTTTGTACAAGAAAGCTGGGTG*CTT*TGTGGAGAAAGTCACAAAGCA-3´.
587 The italicized nucleotides denote the mutated stop codon. The amplicon was then cloned into
588 the pDONR221 vector by BP recombination to generate the middle entry pME-sema7a^{sec}
589 vector. To generate the hsp70:sema7a^{sec}-mKate2 construct, gateway cloning was performed
590 by combining the plasmids p5E-hsp70 (49), pME-sema7a^{sec}, p3E-mKate2-myc no-pA
591 (Addgene, 80812), and pDESTtol2pACrymCherry (Addgene, 64023) with LR Clonase II Plus
592 (Invitrogen). Verified constructs (25 ng/µl plasmid DNA) were injected with Tol2 Transposase
593 mRNA (approximately 25 ng/µl) into one-cell embryos. The transiently transgenic larvae—
594 identified by the expression of red fluorescent protein (mCherry) in their lenses—were raised

595 till 3 dpf, heat-shocked in a water bath at 37 ºC for 1 hr, incubated at 28 ºC for 1 hr to allow
596 expression, and subsequently mounted for live imaging.

597 **Transient transgenesis with the hsp70l:sema7a-GPI-2A-mCherry construct.** The *sema7a-*
598 *GPI* coding sequence without the stop codon (*sema7a-GPI*$^{no\text{-}stop}$) was synthesized using
599 gBlocks HiFi Gene Fragments (Integrated DNA Technologies). The *sema7a-GPI*$^{no\text{-}stop}$ coding
600 sequence was then cloned into the pDONR221 vector by BP recombination to generate the
601 middle entry pME-sema7a-GPI$^{no\text{-}stop}$ vector, henceforth denoted as pME-sema7a-GPI. To
602 generate the hsp70:sema7a-GPI-2A-mCherry construct, gateway cloning was performed by
603 combining the plasmids p5E-hsp70 (49), pME-sema7a-GPI, p3E-2A-mcherrypA (Addgene,
604 26031), and pDESTtol2pACryGFP (Addgene, 64022) with LR Clonase II Plus (Invitrogen).
605 Verified constructs (25 ng/µl plasmid DNA) were injected with Tol2 Transposase mRNA
606 (approximately 25 ng/µl) into one-cell embryos. The transiently transgenic larvae—identified
607 by the expression of green fluorescent protein (GFP) in their lenses—were raised till 3 dpf,
608 heat-shocked in a water bath at 37 ºC for 1 hr, incubated at 28 ºC for 1 hr to allow expression,
609 and subsequently mounted for live imaging.

610 **Microscopy and volumetric rendering of living neuronal arbors and cells.** Living larvae
611 were dechorionated, anaesthetized in 600 µM 3-aminobenzoic acid ethyl ester
612 methanesulfonate in system-water with 1 µg/mL methylene blue, and mounted in 1 % low-
613 melting-point agarose on a glass-bottom MetTek dish at specific stages. The larvae were
614 maintained at 28 °C during imaging in a temperature-controlled stage top chamber (OKO Lab
615 UNO-T). Static images at successive focal depths were captured at 200 nm intervals and
616 deconvolved with Microvolution software in ImageJ (NIH). For time-lapse video microscopy,
617 the ectopic *sema7a*^{sec} integration sites were imaged at intervals of 5 min as Z-stacks acquired
618 with 1.0 µm steps with laser excitation at 488 nm and 561 nm under a 60X, silicone-oil objective
619 lens of numerical aperture 1.30. The three-dimensional datasets were processed and volume-
620 rendered with the surface evolver and filament-tracer tools in Imaris (Bitplane, Belfast, UK).

621 The Imaris workstation was provided by the Rockefeller University Bio-imaging Resource
622 Center.

623 **Generation of pseudocolored trajectories of the dwell times of sensory neurites at the**
624 **ectopic Sema7A^{sec} sources.** Fluorescent intensity values of the sensory neurites and the
625 ectopic Sema7A^{sec} sources were measured from the maximal-intensity projections at each time
626 during the time-lapse video microscopy. The intensity values were normalized and binarized
627 before summing across each timepoint for locations across the XY plane. The resulting
628 pseudocolored trajectories represent the dwell times of the neurites and the Sema7A^{sec} cells
629 through the 10 hr time-lapse video sequence.

630 **Generation of skeletonized networks.** The labeled sensory axons were traced in three
631 dimensions with ImageJ's semi-automated framework, SNT (50). Each trace depicts the
632 skeletonized form of the posterior lateral-line nerve, the posterior lateral-line branch, and the
633 point of arborization from which the sensory arbors radiate to contact the hair cells
634 (Figure 2D,E; Figure 2—figure supplement 2B. The three-dimensional pixels or voxels
635 obtained from the skeletonized sensory arbor traces were processed using custom code written
636 in Python for visual representation and quantitative analysis.

637 **Generation of combined hair cell clusters and the corresponding combined skeletonized**
638 **networks.** The hair cell clusters of neuromasts from each developmental stage were aligned
639 by the centers of their apices, which were identified by the hair bundles, and overlayed to
640 generate combined hair cell clusters (Figure 2—figure supplement 1E,F) using custom Python
641 code. The associated skeletonized sensory-arbor traces at each developmental stage were
642 aligned similarly using custom Python code. The details of the procedures are available upon
643 request and the corresponding code is available on GitHub.

644 **Quantification of sensory arbor distributions around hair cell clusters.** The region from
645 the center of the combined hair cell cluster to 60 μm in the post-cluster region was divided into
646 3600 concentric sections of equal area. Each section, as depicted with a distinct color shade,

647 had an area of π μm^2. Sensory arbor density was defined as Log_{10}[(Area occupied by the arbors
648 in each section)/ (Area of each section)]. The arbor density was then plotted as a histogram
649 against distance from the center of the combined hair cell cluster. Each bin of the histogram
650 represents an area of π μm^2 (Figure 2—figure supplement 2A). The histograms were finally
651 represented as density trace graphs with Kernel Density Estimation (KDE) in Python.

652 **Quantification of contact between sensory arbors and hair cell clusters.** For each hair cell
653 cluster, the voxels of the sensory arbor traces that were inside or within 0.5 μm—the average
654 neurite radius—of the cluster boundary were denoted as arbors in contact with their
655 corresponding hair cell cluster (Figure 2—figure supplement 2B). The percentage of arbors in
656 contact with each hair cell cluster was defined as: (Number of voxels that remained inside the
657 cluster boundary/Total number of voxels in the arbor) X 100. The data were analyzed through
658 an automated pipeline with custom Python code.

659 **Quantification of the sensory arborization network topology.** We developed a custom
660 Python script (snt_topology.py; available on GitHub) to convert the skeletonized sensory
661 arborization networks to network graphs (NetworkX, v3.1). We first used a custom ImageJ
662 macro to convert SNT skeletons to csv files, then generated the network graph from the
663 individual arbor paths. As noted previously, we defined five topological attributes: (1) nodes—
664 junctions where arbors branch, converge, or cross; (2) loops—minimal arbor cycles forming
665 topological holes; (3) bare terminals—arbors with free ends; (4) node degree—the number of
666 first-neighbor nodes incident to a node; and (5) arbor curvature—the total curvature of a bare
667 terminal (Figure 3A). To enumerate loops and quantify their lengths and node numbers, we
668 computed the minimum cycle basis for each network graph. The relative organ height of each
669 node in a graph was defined in 3D using Equation (1):

670 $$(\vec{u} \cdot \vec{v}) \,/\, \|\vec{v}\|^2 , \qquad (1)$$

671 where $\vec{u}$ is the vector from the arborization initiation point to a node and $\vec{v}$ is the vector from the
672 arborization initiation point to the hair cell cluster apex. The relative occurrence of nodes (Figure

673 3—figure supplement 1A-C) was normalized by both the number of hair cells per neuromast
674 and the total number of neuromasts, for comparison across ages and genotypes. The relative
675 number of bare terminals and loops (Figure 3B; Figure 3—figure supplement 1D, E) was
676 normalized by the number of hair cells per neuromast and scaled between 0 and 1. The density
677 was then normalized by the total number of neuromasts imaged for each developmental stage
678 and genotype. For Figure 3C and Figure 3—figure supplement 1F and G, the normalized
679 occurrence was computed as the number of arbors of a given length that formed either a bare
680 terminal or a loop, divided by the total number of arbors of either feature of that length. Lastly,
681 we defined bare terminals as having either high or low curvature (Figure 3F; Figure 3—figure
682 supplement 2E,F) if their absolute total signed curvature [Equation (2)] in three dimensions was
683 either higher or lower than $\pi/6$, respectively:

684 $$\left|\int \frac{dT}{ds} \cdot N(s)\, ds\right|, \tag{2}$$

685 where s is the arc-length parameter of the bare terminal, $T(s)$ is the unit tangent vector at each
686 point along the arbor, $N(s)$ is the unit normal vector at each point, and the integral is evaluated
687 from the terminal's branching node to the arbor's tip. For a closed curve forming a full loop, this
688 value will equal 2π. In practice, we first fit B-splines (scipy.interpolate.splprep; SciPy, v1.10.1)
689 in 3D to the skeletons for each bare terminal before evaluating their derivatives
690 (scipy.interpolate.splev) and integrating (scipy.integrate.simpson) over their lengths.

691 **Quantification of aberrant sensory arborization in ectopic Sema7A^{sec} expression.** The
692 sensory arbor networks were traced in three dimensions with SNT. The surface of each of the
693 ectopically expressing Sema7A^{sec}-mKate2 cells was represented by a single point that was
694 closest to the terminal point of the guided neurite. Distances between two points were
695 calculated using standard mathematical operations.

696 **Quantification of presynaptic and postsynaptic assembly number and area.** Maximal-
697 intensity projections of consecutive through-focus scans encompassing the entire neuromast
698 of control and *sema7a*$^{-/-}$ mutant larvae at 2 dpf, 3 dfp, and 4 dpf were utilized to capture the

presynaptic and postsynaptic assemblies. The number of the synaptic densities across genotypes were measured using ImageJ's cell counter framework. Area of the synaptic densities from the maximal-intensity projections were measured using ImageJ's polygon selection tool (Figure 6—figure supplement 2A-D).

Quantification of the distribution of postsynaptic aggregates along the loops and the bare terminals of the sensory arbor networks. Four-day-old *TgBAC(neurod1:EGFP)* larvae were fixed and stained for sensory arbors and postsynaptic aggregates marked by GFP and MAGUK, respectively. The GFP-positive sensory arbors were traced in three dimensions with ImageJ's semi-automated framework, SNT. The topological attributes of the arbor network, such as the loop and the bare terminal, were determined as described previously. The localizations of the MAGUK punctae along the three-dimensional arbor network were measured using ImageJ's cell counter framework (Figure 6—figure supplement 2E,F). We measured 567 MAGUK punctae from 16 sensory arbor networks. Whether the MAGUK-punctae were associated with a loop or a bare terminal, we categorized them in two groups and quantified their distribution across 16 neuromasts.

Quantification of the distribution of postsynaptic-aggregate density along the distance from the nearest node. The three-dimensional space surrounding each node of the arbor network were divided into concentric shells of equal volume (Figure 6—figure supplement 2E, F). For each node, we computationally generated 100,000 concentric shells that reached a 10 μm radius. We measured the number of MAGUK punctae located within each of those concentric shells from their nearest nodes.

Statistical analysis. Data visualization and statistical analysis were conducted with GraphPad Prism (Version 9) and Python (v3.10). The Mann-Whitney test was used for hypothesis testing unless otherwise noted, and the statistical details are given in the respective figure legends.

Data and code availability. Owing to size restrictions, the experimental image data have not been uploaded to a repository but are available from the corresponding author on request. The

codes generated during this study are available on GitHub (https://github.com/agnikdasgupta/Sema7A_regulates_neural_circuitry).

Acknowledgments. The authors thank Nicolas Velez and Emily Atlas for valuable discussions. Samantha Campbell and Anna Kaczynska provided expert fish husbandry. Katie Kindt kindly provided various strains of zebrafish. Image processing benefitted from facilities at the Bio-Imaging Resource Center. A.D. was supported by a Kavli Neural Systems Institute Postdoctoral Fellowship from The Rockefeller University. C.C.R. is supported by National Science Foundation Graduate Research Fellowship Grant No. 1946429. A.J., S.P.P., and L.M.S. were supported by Howard Hughes Medical Institute, of which A.J.H. is an Investigator.

Author Contributions

A.D. initiated the project, conducted experiments, analyzed data, and quantified results. C.C.R developed the Python codes for the network topology analysis and quantified those results, as well as analyzed published transcriptomics data. S.P.P. developed the Python codes for three-dimensional visual representation of sensory arbors and quantified arbor morphologies. L.M.S. conducted preliminary experiments. A.J. plotted Sema7A intensity measurements. A.D. wrote the paper with contributions from C.C.R and A.J.H.

Declaration of Interests

The authors declare no competing interests.

References

1. Lykissas M, Batistatou A, Charalabopoulos K, Beris A. The Role of Neurotrophins in Axonal Growth, Guidance, and Regeneration. Curr Neurovasc Res. 2007 May 1;4(2):143–51.

2. Vaccaro G, Dumoulin A, Zuñiga NR, Bandtlow CE, Stoeckli ET. The Nogo-66 Receptors NgR1 and NgR3 Are Required for Commissural Axon Pathfinding. J Neurosci. 2022 May 18;42(20):4087–100.

750 3. Nguyen-Ba-Charvet KT, Di Meglio T, Fouquet C, Chedotal A. Robos and Slits Control the
751 Pathfinding and Targeting of Mouse Olfactory Sensory Axons. J Neurosci. 2008 Apr
752 16;28(16):4244–9.

753 4. Jeroen Pasterkamp R, Peschon JJ, Spriggs MK, Kolodkin AL. Semaphorin 7A promotes
754 axon outgrowth through integrins and MAPKs. Nature. 2003 Jul;424(6947):398–405.

755 5. Nagiel A, Andor-Ardo D, Hudspeth AJ. Specificity of Afferent Synapses onto Plane-
756 Polarized Hair Cells in the Posterior Lateral Line of the Zebrafish. J Neurosci. 2008 Aug
757 20;28(34):8442–53.

758 6. Jacobo A, Dasgupta A, Erzberger A, Siletti K, Hudspeth AJ. Notch-Mediated Determination
759 of Hair-Bundle Polarity in Mechanosensory Hair Cells of the Zebrafish Lateral Line. Curr
760 Biol. 2019 Nov;29(21):3579-3587.e7.

761 7. Valera G, Markov DA, Bijari K, Randlett O, Asgharsharghi A, Baudoin JP, et al. A neuronal
762 blueprint for directional mechanosensation in larval zebrafish. Curr Biol. 2021
763 Apr;31(7):1463-1475.e6.

764 8. Dow E, Jacobo A, Hossain S, Siletti K, Hudspeth AJ. Connectomics of the zebrafish's
765 lateral-line neuromast reveals wiring and miswiring in a simple microcircuit. eLife. 2018 Jun
766 12;7:e33988.

767 9. Lush ME, Diaz DC, Koenecke N, Baek S, Boldt H, St Peter MK, et al. scRNA-Seq reveals
768 distinct stem cell populations that drive hair cell regeneration after loss of Fgf and Notch
769 signaling. eLife. 2019 Jan 25;8:e44431.

770 10. Carulli D, de Winter F, Verhaagen J. Semaphorins in Adult Nervous System Plasticity
771 and Disease. Front Synaptic Neurosci. 2021 May 11;13:672891.

772 11. Yazdani U, Terman JR. The semaphorins. Genome Biol. 2006;7(3):211.

773 12. de Winter F, Kwok JCF, Fawcett JW, Vo TT, Carulli D, Verhaagen J. The
774 Chemorepulsive Protein Semaphorin 3A and Perineuronal Net-Mediated Plasticity. Neural
775 Plast. 2016;2016:1–14.

776 13. Coate TM, Spita NA, Zhang KD, Isgrig KT, Kelley MW. Neuropilin-2/Semaphorin-3F-
777 mediated repulsion promotes inner hair cell innervation by spiral ganglion neurons. eLife.
778 2015 Aug 24;4:e07830.

779 14. Carcea I, Patil SB, Robison AJ, Mesias R, Huntsman MM, Froemke RC, et al.
780 Maturation of cortical circuits requires Semaphorin 7A. Proc Natl Acad Sci. 2014 Sep
781 23;111(38):13978–83.

782 15. Inoue N, Nishizumi H, Naritsuka H, Kiyonari H, Sakano H. Sema7A/PlxnCl signaling
783 triggers activity-dependent olfactory synapse formation. Nat Commun. 2018
784 Dec;9(1):1842.

785 16. Inoue N, Nishizumi H, Ooyama R, Mogi K, Nishimori K, Kikusui T, et al. The olfactory
786 critical period is determined by activity-dependent Sema7A/PlxnC1 signaling within
787 glomeruli. eLife. 2021 Mar 29;10:e65078.

788 17. Morote-Garcia JC, Napiwotzky D, Köhler D, Rosenberger P. Endothelial Semaphorin
789 7A promotes neutrophil migration during hypoxia. Proc Natl Acad Sci. 2012 Aug
790 28;109(35):14146–51.

791 18. Nishide M, Kumanogoh A. The role of semaphorins in immune responses and
792 autoimmune rheumatic diseases. Nat Rev Rheumatol. 2018 Jan;14(1):19–31.

793 19. Köhler D, Granja T, Volz J, Koeppen M, Langer HF, Hansmann G, et al. Red blood
794 cell-derived semaphorin 7A promotes thrombo-inflammation in myocardial ischemia-
795 reperfusion injury through platelet GPIb. Nat Commun. 2020 Dec;11(1):1315.

796 20. Pham TL, He J, Kakazu AH, Jun B, Bazan NG, Bazan HEP. Defining a mechanistic
797 link between pigment epithelium–derived factor, docosahexaenoic acid, and corneal nerve
798 regeneration. J Biol Chem. 2017 Nov;292(45):18486–99.

799 21. Xie J, Wang H. Semaphorin 7A as a potential immune regulator and promising
800 therapeutic target in rheumatoid arthritis. Arthritis Res Ther. 2017 Dec;19(1):10.

801 22. Baek S, Tran NTT, Diaz DC, Tsai YY, Acedo JN, Lush ME, et al. Single-cell
802 transcriptome analysis reveals three sequential phases of gene expression during
803 zebrafish sensory hair cell regeneration. Dev Cell. 2022 Mar 28;57(6):799-819.e6.

804 23. Dow E, Siletti K, Hudspeth AJ. Cellular projections from sensory hair cells form
805 polarity-specific scaffolds during synaptogenesis. Genes Dev. 2015 May 15;29(10):1087–
806 94.

807 24. Pujol-Martí J, Faucherre A, Aziz-Bose R, Asgharsharghi A, Colombelli J, Trapani JG,
808 et al. Converging Axons Collectively Initiate and Maintain Synaptic Selectivity in a
809 Constantly Remodeling Sensory Organ. Curr Biol. 2014 Dec;24(24):2968–74.

810 25. De Wit J, De Winter F, Klooster J, Verhaagen J. Semaphorin 3A displays a punctate
811 distribution on the surface of neuronal cells and interacts with proteoglycans in the
812 extracellular matrix. Mol Cell Neurosci. 2005 May;29(1):40–55.

813 26. Dalle Nogare DE, Natesh N, Vishwasrao HD, Shroff H, Chitnis AB. Zebrafish Posterior
814 Lateral Line primordium migration requires interactions between a superficial sheath of
815 motile cells and the skin. eLife. 2020 Nov 25;9:e58251.

816 27. Ji YR, Warrier S, Jiang T, Wu DK, Kindt KS. Directional selectivity of afferent neurons
817 in zebrafish neuromasts is regulated by Emx2 in presynaptic hair cells. eLife. 2018 Apr
818 19;7:e35796.

819 28. Diaz-Horta O, Abad C, Sennaroglu L, Foster J, DeSmidt A, Bademci G, et al. ROR1 is
820 essential for proper innervation of auditory hair cells and hearing in humans and mice. Proc
821 Natl Acad Sci U S A. 2016 May 24;113(21):5993–8.

822 29. Newman M. The structure of real-world networks [Internet]. Vol. 1. Oxford University
823 Press; 2018 [cited 2023 May 2]. Available from:
824 https://academic.oup.com/book/27884/chapter/203817512

825 30. Sharma P, Ruel TD, Kocha KM, Liao S, Huang P. Single cell dynamics of embryonic
826 muscle progenitor cells in zebrafish. Development. 2019 Jan 1;dev.178400.

827 31. Keenan SR, Currie PD. The Developmental Phases of Zebrafish Myogenesis. J Dev
828 Biol. 2019 Jun 2;7(2):12.

829 32. Sato A, Koshida S, Takeda H. Single-cell analysis of somatotopic map formation in the
830 zebrafish lateral line system. Dev Dyn. 2010 Jul;239(7):2058–65.

831 33. Shen K, Cowan CW. Guidance Molecules in Synapse Formation and Plasticity. Cold
832 Spring Harb Perspect Biol. 2010 Apr 1;2(4):a001842–a001842.

833 34. Um JW, Ko J. Neural Glycosylphosphatidylinositol-Anchored Proteins in Synaptic
834 Specification. Trends Cell Biol. 2017 Dec;27(12):931–45.

835 35. Uesaka N, Uchigashima M, Mikuni T, Nakazawa T, Nakao H, Hirai H, et al. Retrograde
836 semaphorin signaling regulates synapse elimination in the developing mouse brain.
837 Science. 2014 May 30;344(6187):1020–3.

838 36. Sheets L, Hagen MW, Nicolson T. Characterization of Ribeye Subunits in Zebrafish
839 Hair Cells Reveals That Exogenous Ribeye B-Domain and CtBP1 Localize to the Basal
840 Ends of Synaptic Ribbons. Riley B, editor. PLoS ONE. 2014 Sep 10;9(9):e107256.

841 37. Oliva C, Escobedo P, Astorga C, Molina C, Sierralta J. Role of the maguk protein
842 family in synapse formation and function. Dev Neurobiol. 2012 Jan;72(1):57–72.

843 38. Suli A, Pujol R, Cunningham DE, Hailey DW, Prendergast A, Rubel EW, et al.
844 Innervation regulates synaptic ribbons in lateral line mechanosensory hair cells. J Cell Sci.
845 2016 Jan 1;jcs.182592.

846 39. Obholzer N, Wolfson S, Trapani JG, Mo W, Nechiporuk A, Busch-Nentwich E, et al.
847 Vesicular Glutamate Transporter 3 Is Required for Synaptic Transmission in Zebrafish Hair
848 Cells. J Neurosci. 2008 Feb 27;28(9):2110–8.

849 40. Taschenberger H, Leão RM, Rowland KC, Spirou GA, von Gersdorff H. Optimizing
850 Synaptic Architecture and Efficiency for High-Frequency Transmission. Neuron. 2002
851 Dec;36(6):1127–43.

852 41. Myers JP, Gomez TM. Focal Adhesion Kinase Promotes Integrin Adhesion Dynamics
853 Necessary for Chemotropic Turning of Nerve Growth Cones. J Neurosci. 2011 Sep
854 21;31(38):13585–95.

855 42. O'Donnell M, Chance RK, Bashaw GJ. Axon Growth and Guidance: Receptor
856 Regulation and Signal Transduction. Annu Rev Neurosci. 2009 Jun 1;32(1):383–412.

857 43. Gilmour D, Knaut H, Maischein HM, Nüsslein-Volhard C. Towing of sensory axons by
858 their migrating target cells in vivo. Nat Neurosci. 2004 May;7(5):491–2.

859 44. Metcalfe WK. Sensory neuron growth cones comigrate with posterior lateral line
860 primordial cells in zebrafish. J Comp Neurol. 1985 Aug 8;238(2):218–24.

861 45. Gasanov EV, Rafieva LM, Korzh VP. BDNF-TrkB Axis Regulates Migration of the
862 Lateral Line Primordium and Modulates the Maintenance of Mechanoreceptor Progenitors.
863 Proost P, editor. PLOS ONE. 2015 Mar 9;10(3):e0119711.

864 46. Schuster K, Dambly-Chaudière C, Ghysen A. Glial cell line-derived neurotrophic factor
865 defines the path of developing and regenerating axons in the lateral line system of
866 zebrafish. Proc Natl Acad Sci. 2010 Nov 9;107(45):19531–6.

867 47. Germanà A, Laurà R, Montalbano G, Guerrera MC, Amato V, Zichichi R, et al.
868 Expression of Brain-Derived Neurotrophic Factor and TrkB in the Lateral Line System of
869 Zebrafish During Development. Cell Mol Neurobiol. 2010 Jul;30(5):787–93.

870 48. Kindt KS, Finch G, Nicolson T. Kinocilia Mediate Mechanosensitivity in Developing
871 Zebrafish Hair Cells. Dev Cell. 2012 Aug;23(2):329–41.

872 49. Kwan KM, Fujimoto E, Grabher C, Mangum BD, Hardy ME, Campbell DS, et al. The
873 Tol2kit: A multisite gateway-based construction kit forTol2 transposon transgenesis
874 constructs. Dev Dyn. 2007 Nov;236(11):3088–99.

875 50. Arshadi C, Günther U, Eddison M, Harrington KIS, Ferreira TA. SNT: a unifying
876 toolbox for quantification of neuronal anatomy. Nat Methods. 2021 Apr;18(4):374–7.

877

878 **Figures and Figure Legends**

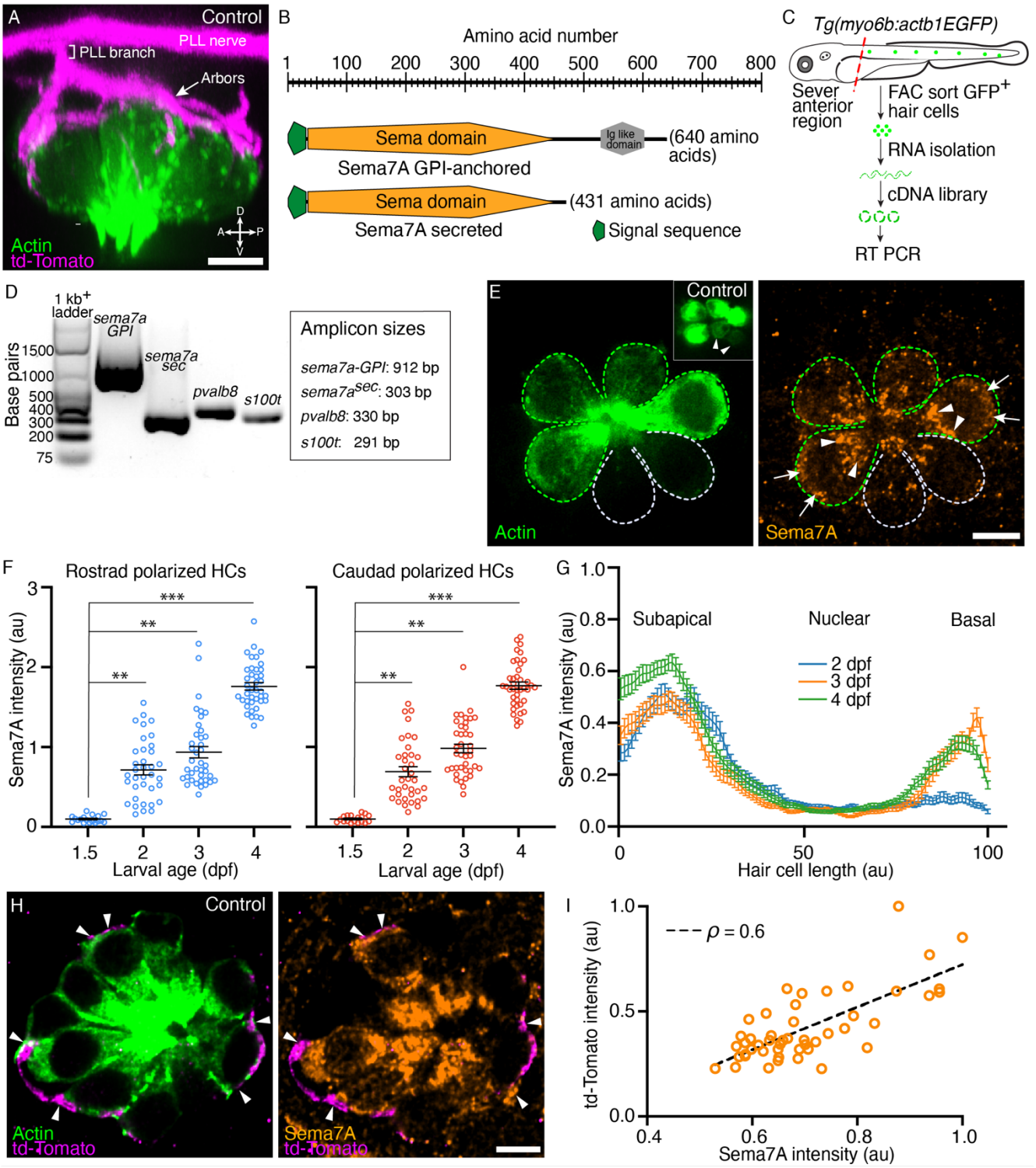

879 **Figure 1. Expression of Semaphorin7A in the zebrafish's lateral line.** (A) A volumetric
880 rendering of a PLL neuromast depicts the sensory axons (magenta) that branch from the lateral
881 line nerve to arborize around the basolateral surface of the hair cell cluster (green). Additional

882 cell types in the neuromast are not labeled. Larval age, 3 dpf. A=anterior, P=posterior,
883 D=dorsal, V=ventral. (B) A schematic drawing of the two variants of the Sema7A protein
884 molecule depicts the full-length GPI-anchored form and the smaller, potentially secreted form.
885 Both the molecules include a signal sequence (green) and a conserved sema domain (orange).
886 (C) *Tg(myo6b:actb1-EGFP)* larvae at 4 dpf were terminally anesthetized and their heads were
887 removed with fine blades. The tails were then dissociated into the component cells, which were
888 sorted by flow cytometry. Green cells represent GFP^+ hair cells. A cDNA library was prepared
889 from the isolated RNA. (D) Gel-based RT-PCR analysis indicates the presence of both the
890 *sema7a* transcript variants and the expression of hair cell-specific genes, parvalbumin 8
891 (*pvalb8*) and S100 calcium binding protein T (*s100t*). (E) A surface micrograph of a neuromast
892 at 3 dpf depicts two pairs of mature hair cells (green dashed lines) and a pair of immature hair
893 cells (grey dashed lines). Inset: among the three pairs of hair cell apices, the immature pair is
894 indicated by arrowheads. Immunolabeling reveals that the Sema7A protein (orange) occurs
895 consistently at the subapical region (arrowheads) and at the basolateral surface (arrows) of a
896 hair cell. In this and in each of the subsequent neuromast images, anterior is to the left and
897 dorsal to the top. (F) A plot quantifies developmental changes in the average Sema7A intensity
898 in both rostrally and caudally polarized hair cells of neuromasts from 1.5 dpf to 4 dpf. The data
899 stem from 18, 36, 39, and 40 hair cells in neuromasts of respectively 1.5 dpf, 2 dpf, 3 dpf, and
900 4 dpf larvae. (G) A plot quantifies the distribution of average Sema7A intensity along the hair
901 cell's apicobasal axis. The results stem from 52, 57, and 54 hair cells of neuromasts from 2 dpf,
902 3 dpf, and 4 dpf larvae. (H) An immunofluorescence image at the nuclear level of a 4 dpf
903 neuromast shows the contact of the sensory arbors (magenta) with the basolateral surface of
904 the hair cells (green). Immunolabeling for Sema7A (orange) reveals enrichment of the protein
905 at the hair cell bases and sensory-axon interfaces (arrowheads). (I) At the base of the hair cell,
906 association of the td-$Tomato^+$ sensory arbors positively correlated with the Sema7A intensity.
907 The results stemmed from 48 hair cells of 13 neuromasts from 3 dpf larvae. HC, hair cell; scale

908 bars, 5 μm; au, arbitrary unit; means ± SEMs; ρ, Spearman's correlation coefficient; *** implies

909 $p < 0.001$ and ** implies $p < 0.01$.

910

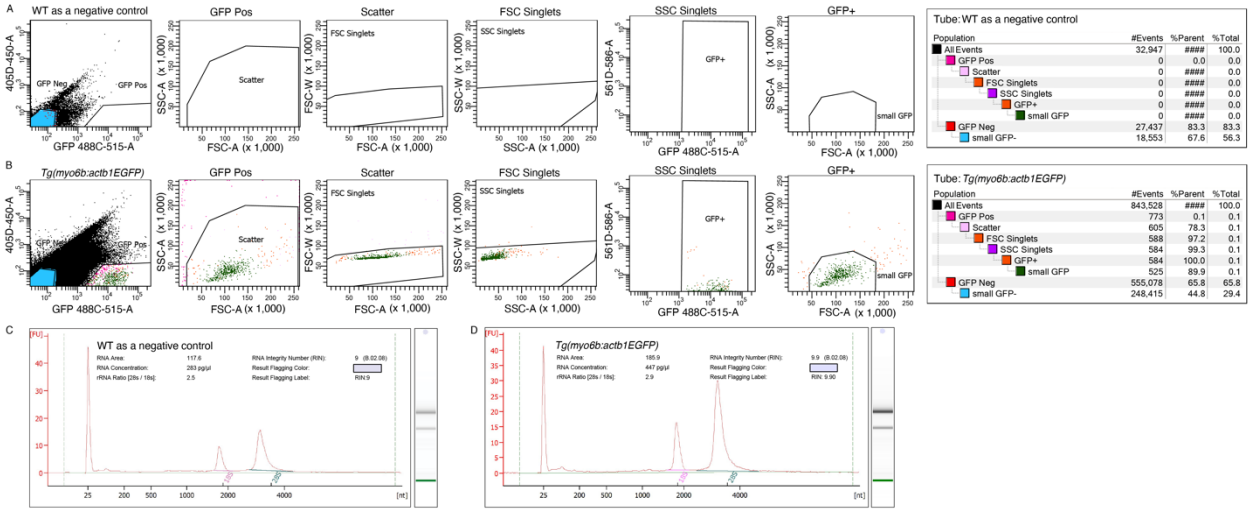

Figure 1—figure supplement 1. Isolation of GFP-expressing hair cells. (A,B) Representative results from florescence-activated cell sorting demonstrate the efficient discrimination of GFP+ (green) hair cells from *Tg(myo6b:actb1-EGFP)* larval tails. Around 400 tails were utilized to isolate hair cells. Wild type (WT) controls confirm the selectivity of the gates. (C,D) Plots represent the RNA integrity numbers (RINs) of the isolated total RNA from WT and transgenic larvae. High RIN values suggest minimal degradation of isolated RNAs from both samples.

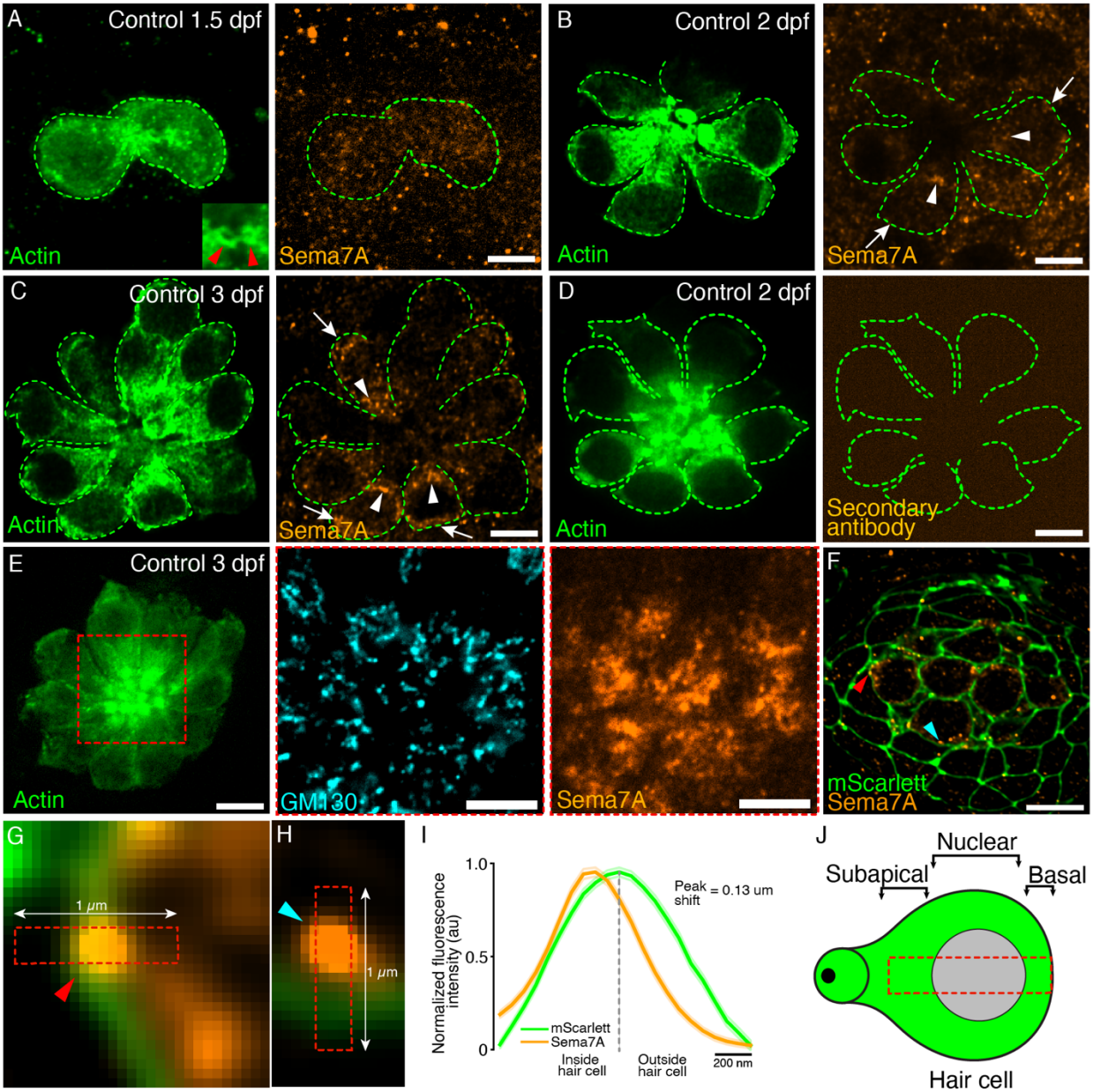

920 **Figure 1—figure supplement 2. Expression of Semaphorin7A in the lateral line**
921 **neuromast.** (A-C) Surface micrographs show hair cells marked with actin-GFP (green dashed
922 lines) and the localization of Sema7A protein (orange) in the subapical (arrowheads) and basal
923 regions (arrows) of the corresponding hair cells from neuromasts of developing control larvae.
924 The inset in panel A (red arrowheads) depicts the apices of the immature hair cell pair.
925 (D) Immunolabeling with only the secondary antibody fails to detect any Sema7A signal. (E) A
926 surface micrograph depicts hair cells (green, left) whose subapical region (red dashed line)
927 harbors the Golgi network–labeled by the Golgi resident protein GM130 (cyan, middle)–where

928 the Sema7A protein is enriched (orange, right). (F) A micrograph at a nuclear plane of a 4 dpf
929 neuromast depicts membrane-tethered Scarlet (green) in all cells of the neuromast and the
930 Sema7A protein (orange, arrowheads) in centrally clustered hair cells. (G) The Sema7A protein
931 is located at the basal membrane (red arrowhead). (H) The Sema7A protein is also observed
932 adjacent to the basal membrane, potentially in a vesicle (cyan arrowhead). (I) A plot quantifies
933 the distribution of average Sema7A intensity across the hair cell's basal membrane. The results
934 stem from 100 hair-cell membranes of 10 neuromasts from 4 dpf larvae. (J) A schematic
935 diagram of a single hair cell depicts the three distinct regions along the apicobasal axis of the
936 cell. Sema7A intensity was measured along this apicobasal axis (red dashed line). Scale bars,
937 5 μm; au, arbitrary unit; means ± SEMs.
938

939

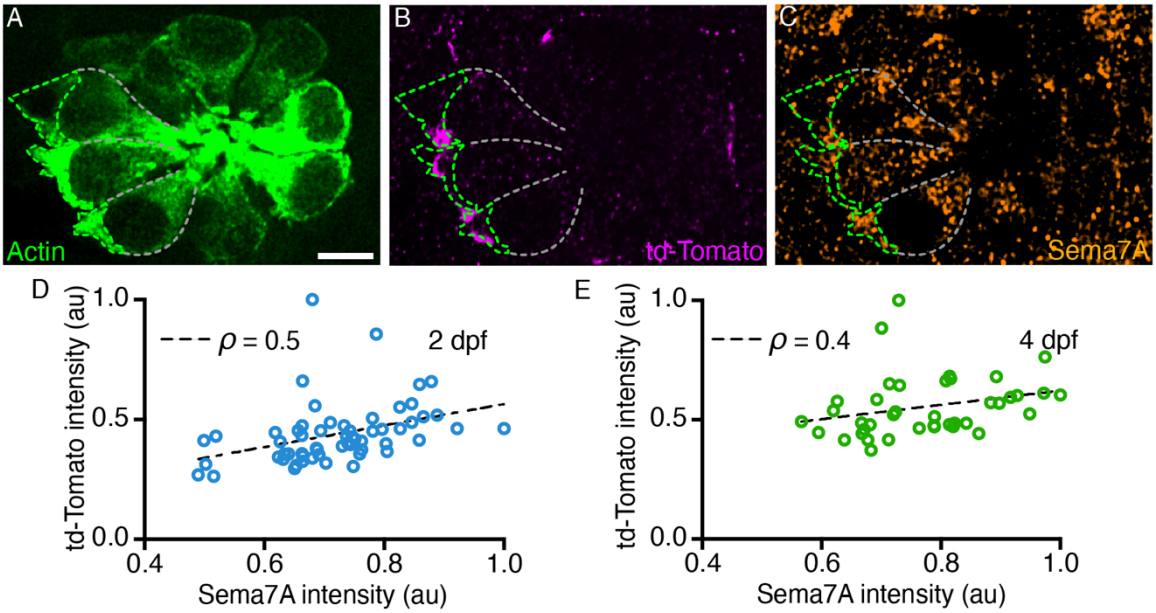

940 **Figure 1—figure supplement 3. Sema7A progressively enriches at the hair cell base with**
941 **the sensory axons.** (A) A micrograph at a nuclear plane of a 3 dpf neuromast depicts several
942 actin-GFP (green) labeled hair cells. The lateral (white dashed line) and the basal (green
943 dashed line) surfaces of three hair cells are outlined. (B) The td-Tomato-positive sensory arbors
944 contact the basal regions (green dashed line) of three hair cells. (C) The Sema7A is enriched
945 in the basal regions (green dashed line) of the hair cells that are in contact with the sensory
946 arbors. (D,E) At the base of the hair cell, intensities of the td-Tomato-positive sensory arbors
947 positively correlate with the Sema7A intensities. The results stem from 66 hair cells of 15
948 neuromasts from 2 dpf larvae and 40 hair cells of 11 neuromasts from 4 dpf larvae. Scale bars,
949 5 μm; au, arbitrary unit; ρ, Spearman's correlation coefficient.
950

```
Mus             MTPPPPGRAAPSAPRARVLSLPARFGLPLRLRLLLVFWVAAASAQGHSRSGPRISAVWKG
Danio           -------------------MIRHYSSLKFKGNLAYPWLIYGACFQCVFCSCNPRLTLKQD
                                    :    .* :: .*   : : .*. *    *     :: :.

Mus             QDHVDFSQPEPHTVLFHEPGSFSVWVGGRGKVYHFNFPEGKNASVRTVNIGSTKGSCQDK
Danio           NAPLNYNTNYSHTVLFHEEGSKSLFVGGSNIVLHFDVDSYEILENFTLNANLPR---CGE
                :  :::.   .******* ** *::*** . * **:. . :  .  *:* . .:    .:

Mus             QDCGNYITLLERRGNGLLVCGTNARKPSCWNLVN---DSVMMSLGEMKGYAPFSPDENSL
Danio           SSCENVVTVIETFQNCKFVCGTNGEEPQCWELYPRESNHSVVKSVEGTGISPHSSEQNSL
                ..* * :*::*   *  :*****..:*.**:*     :  ::.  * .* :*.*.::***

Mus             VLFEGDEVYSTIRKQEYNGKIPRFRRIRGESELYTSDTVMQNPQFIKATIVH-QDQAYDD
Danio           SLVADGDLYAAAPLYSDGTLLQFRRKAGKRINVWMHDQWVSEPTFISSFLAKRKNDSLNE
                 *. ..::*::    . .  :   *:   . :::  *  :.:* **.: :.: :::: ::

Mus             KIYYFFREDNPDKNPEAPLNVSRVAQLCRGDQGGESSLSVSKWNTFLKAMLVCSDAATNR
Danio           KIYVLFREKNSDTSPEADPWISRVARVCKIDEGGSKQFLQNIWTSFLKARLVCGIPKESL
                *** :***.*.*..***   :****::*: *:**...:  . *.:**** ***. .  .

Mus             NFNRLQDVFLLPDPSGQWRDTRVYGVFSNPWNYSAVCVYSLGDIDRVFRTSSLKGYHMGL
Danio           YFNRLQDVFVQH--AEDWRDSLVYALFSSSWNSTAVCIYSLADLDDIFEKSNYKGFSEAI
                 ********:    : :***: **.:**..** :***:***.*:* :*..*. **:  .:

Mus             PNPRPGMCLPKKQPIPTETFQVADSHPEVAQRVEPMGPLKTPLFHSKYHYQKVVVHRMQA
Danio           PNPRPGKCVENSNSLPIPTLKIIKDYPEMKDWIHPIQ-KDTPFFTSSKNFTKIVVDQIRA
                ****** *: :.:.:*  *::: ..:**: : :.*:   .**:* *. :: *:**.:::*

Mus             SNGETFHVLYLTTDRGTIHKVVESGDQDHSFVFNIMEIQPFHRAAAIQAISLDADRRKLY
Danio           LDENVYNVLLLATDDGMIFKILQHG----SKPFIISETHLCNGCAPIQSMKLDSKKRKLF
                 : :.::** *:** * *.*::: *    *  * * * :  : .*.**::.**:.:***:

Mus             VTSQWEVSQVPLDMCEVYSGGCHGCLMSRDPYCGWDQDRCVSIYSS--QRSVLQSINPAE
Danio           VGYPGQMSVLELQRCQDYGASCEECVLSRDPYCAWSEKGCTSQTRGGIQNISDGNVTKVC
                *    ::* : *: *: *...*. *::******.*.:. *.*   .  *.    .:. .

Mus             PHRECPNPKPDE------APLQKVSLARNSRYYLTCPMESRHATYLWRHEENVEQSCEPG
Danio           DHKSVGRVRRDAQQSSTAPSRIQHTVATDVPFYLSCPVDSHHASYRWEHGG---KSNPCQ
                 *:.  . : *       ..  : ::* :  :**:**::*:**:* *.*     :*

Mus             HQSPSCILFIENLTARQYGHYRCEAQEGSYLREAQHWELLPE-DRALAEQLMGHARALAA
Danio           QTQSEYLLLIPAMTAENYGNYSCVSQERDYIKVVREYELLAKSVFNDAFKLKIQDRQLMV
                : ... :*:*  :**.:**:* * :** .*:: .:.:***.:     * :*  : * * .

Mus             SFWLGVLPTLILGLLVH
Danio           AFVTSAFYLCSL-----
                :*  ..:    *
```

Sequence 1: Mus musculus 664 aa
Sequence 2: Danio rerio 640 aa
Immunogen: Mouse myeloma cell line NS0-derived recombinant mouse Semaphorin 7A Glutamine 45 to Alanine 646. The corresponding region in the zebrafish's Semaphorin 7A is represented by Glutamine 26 to Methionine 627. We predict that the antibody recognizes both variants of the *sema7a* encoded proteins. The Sema domains in both mouse and zebrafish are highlighted in orange.

Figure 1—figure supplement 4. Alignment of the mouse and the zebrafish Sema7A protein sequences generated by Clustal Omega. (A) Multiple sequence alignment depicts the conserved Sema domain (orange) and the immunogenic region for the Sema7A antibody in mouse, and its equivalent region in zebrafish.

956 **Video 1. Sema7A is enriched at the hair cell base and sensory-axon interface**. A through-
957 focus scan of a 4 dpf control neuromast depicts the hair cells (green) that are innervated by the
958 sensory axons (magenta) at their basolateral surfaces where the Sema7A protein (orange) is
959 highly enriched. Scale bar, 5 μm.
960

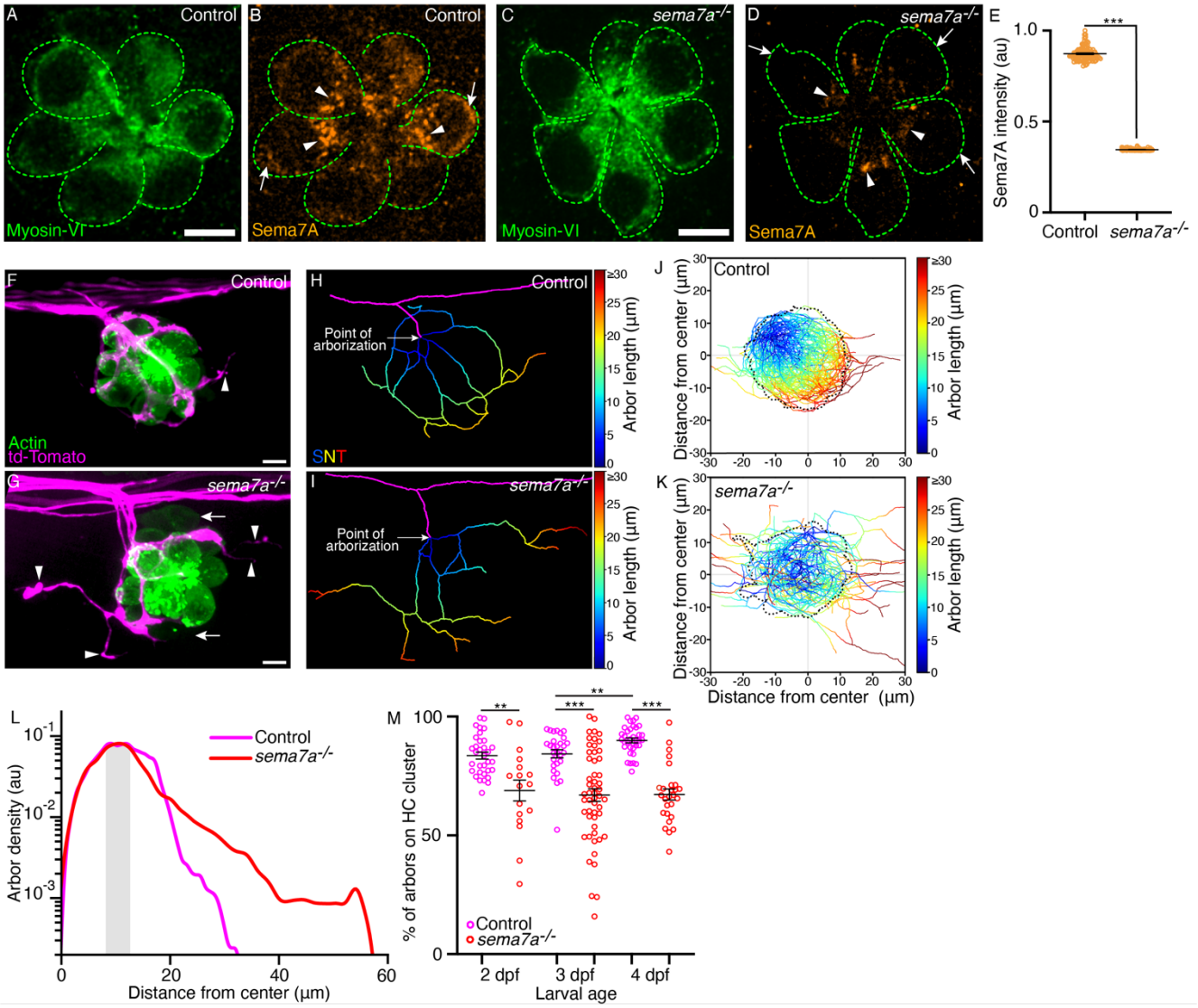

Figure 2. *sema7a*$^{-/-}$ mutants display aberrant sensory axon arborizations. (A-D) In micrographs of 3 dpf control and *sema7a*$^{-/-}$ neuromasts, Myosin VI (green) marks the hair cells (green dashed lines). The level of Sema7A (orange) is highly reduced in the *sema7a*$^{-/-}$ mutant compared to the control, with sporadic localization in the subapical region (arrowheads) and none in the basolateral (arrow) region. (E) A plot of normalized Sema7A intensity from 99 control and 100 *sema7a*$^{-/-}$ hair cells quantitates the effect. (F,G) Surface views of a control and a *sema7a*$^{-/-}$ neuromast at 4 dpf depict the interaction of the sensory arbors (magenta) with hair cell clusters (green). In the control, the arbors intimately contact the hair cells, with a few exceptions (arrowhead). In the *sema7a*$^{-/-}$ mutant, the arbors direct many aberrant projections

970 (arrowheads) away from the hair cell cluster. The two immature hair cell pairs in the *sema7a*$^{-/-}$
971 neuromast are indicated by arrows. (H,I) Skeletonized networks portray the three-dimensional
972 topology of the sensory arbors from the control and the *sema7a*$^{-/-}$ neuromasts depicted in
973 panels F and G, respectively. The pseudocolored trajectories depict the increase in arbor
974 contour length from each point of arborization, defined as the point at which the lateral line
975 branch (magenta) contacts hair cell cluster. (J,K) Micrographs depict the skeletonized networks
976 of the combined 4 dpf hair cell clusters, whose centers are located at (0,0). The X- and
977 Y-coordinates represent the anteroposterior (AP) and the dorsoventral (DV) axes of the larva,
978 respectively. Positive values of the X- and Y-coordinates represent the posterior and ventral
979 directions, respectively. Combined skeletonized network traces from 27 control and 27
980 *sema7a*$^{-/-}$ mutant neuromasts are represented. (L) The plot denotes the densities of the
981 sensory arbors around the center of the combined hair cell clusters for 35 control (magenta)
982 and 27 *sema7a*$^{-/-}$ (red) neuromasts at 4 dpf. The shaded area marks the region proximal to the
983 boundary of the combined hair cell cluster. (M) The plot quantifies the degree of contact of the
984 sensory arbors to their hair cell clusters in individual neuromasts from both control (magenta)
985 and *sema7a*$^{-/-}$ mutants (red), each point represents a single neuromast. Thirty-three, 29, and
986 35 neuromasts were analyzed from 2 dpf, 3 dpf, and 4 dpf control larvae, respectively.
987 Seventeen, 53, and 27 neuromasts were analyzed from 2 dpf, 3 dpf, and 4 dpf
988 *sema7a*$^{-/-}$ mutant larvae, respectively. HC, hair cell; Scale bars, 5 μm; au, arbitrary unit;
989 means ± SEMs; *** signifies $p < 0.001$; ** signifies $p < 0.01$.
990

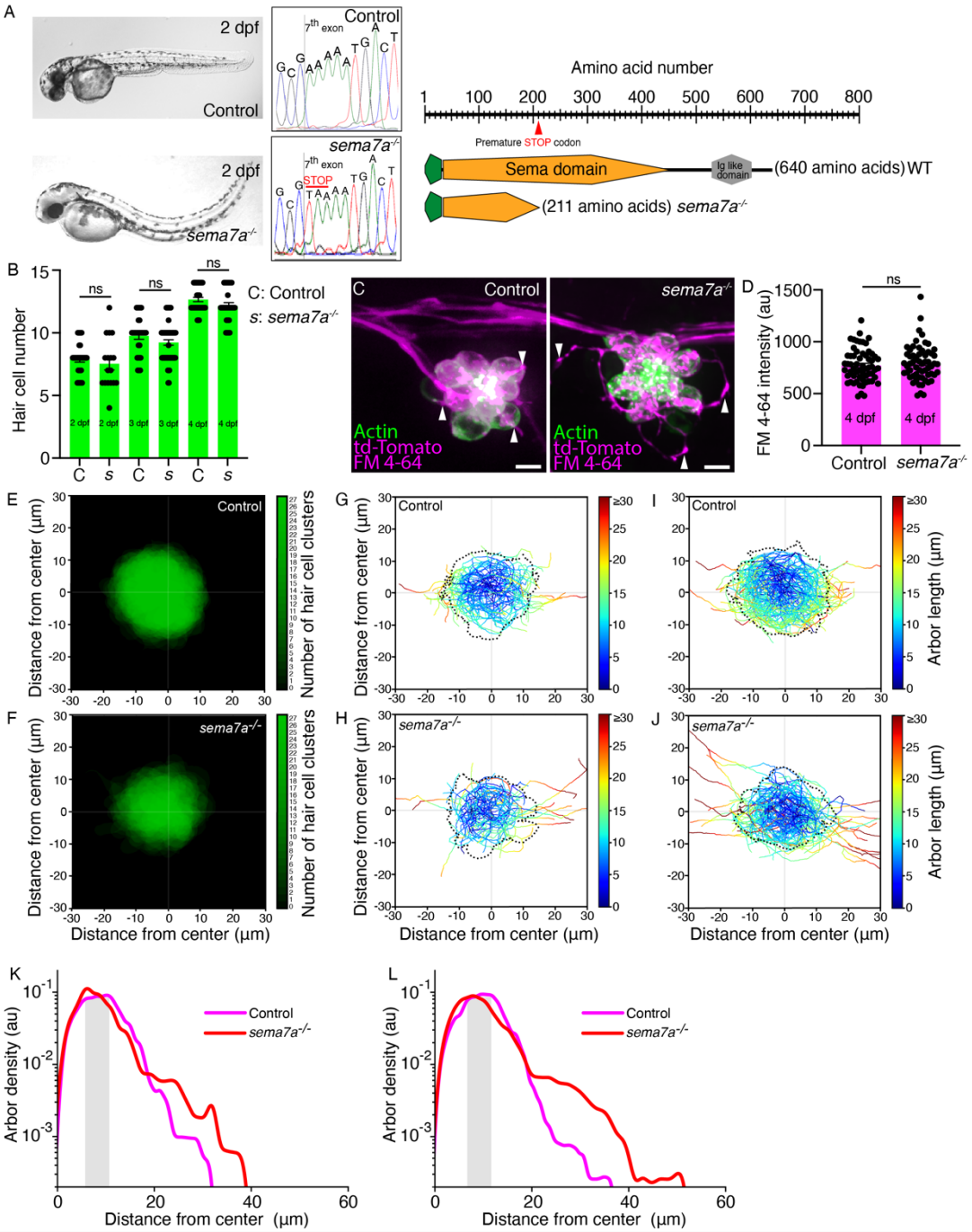

Figure 2—figure supplement 1. *sema7a*$^{-/-}$ mutants exhibit aberrant sensory-axon arborization throughout development. (A) Micrographs depict the overall morphologies and *sema7a* genomic profiles of 2 dpf control (top) and *sema7a*$^{-/-}$ larvae (bottom). The schematic diagram on the right depicts the mutation site and the resulting early truncation of the encoded protein. (B) The plot quantitates the number of hair cells from 33, 29, and 35 neuromasts from 2 dpf, 3 dpf, and 4 dpf control larvae, respectively and 17, 53, and 27 neuromasts from 2 dpf,

1013 3 dpf, and 4 dpf *sema7a*$^{-/-}$ mutant larvae, respectively. No significant change in hair cell number
1014 was observed between the control and the *sema7a*$^{-/-}$ neuromasts across developmental
1015 stages. (C) Micrographs depict maximum intensity projections of 4 dpf neuromasts from control
1016 and *sema7a*$^{-/-}$ larvae where the hair cells (green) are stained with FM 4-64 (magenta). The
1017 sensory arbors (arrowheads, magenta) tightly enwrap the clustered hair cells in the control
1018 neuromast but show aberrant arborization in the *sema7a*$^{-/-}$ larvae. (D) The plot quantitates the
1019 average FM 4-64 intensities from the hair cells of the control and the *sema7a*$^{-/-}$ neuromasts.
1020 (E,F) Micrographs depict combined 4 dpf hair cell clusters, each of whose centers arise located
1021 at (0,0). The X- and Y-coordinates represent the anteroposterior (AP) and dorsoventral (DV)
1022 axes of the larva, respectively. Positive values of the X- and Y-coordinates represent posterior
1023 and ventral directions, respectively. Combined hair cell clusters from 27 control and 27
1024 *sema7a*$^{-/-}$ mutant neuromasts are represented. (G,H) Micrographs depict the skeletonized
1025 networks of the combined 2 dpf hair cell clusters from 17 control and 17 *sema7a*$^{-/-}$ mutant
1026 neuromasts. (I,J) Micrographs depict the skeletonized networks of the combined 3 dpf hair cell
1027 clusters from 29 control and 29 *sema7a*$^{-/-}$ mutant neuromasts. (K) A plot quantitates the
1028 densities of the sensory arbors around the center of the combined hair cell clusters for 33
1029 control (magenta) and 17 *sema7a*$^{-/-}$ (red) neuromasts at 2 dpf. The shaded area marks the
1030 region proximal to the boundary of the combined hair cell cluster. (L) A plot quantitates the
1031 densities of the sensory arbors around the center of the combined hair cell clusters for 29
1032 control (magenta) and 53 *sema7a*$^{-/-}$ (red) neuromasts at 3 dpf. The shaded area marks the
1033 region proximal to the boundary of the combined hair cell cluster. Scale bars, 5 μm; au, arbitrary
1034 units; ns, not significant.
1035

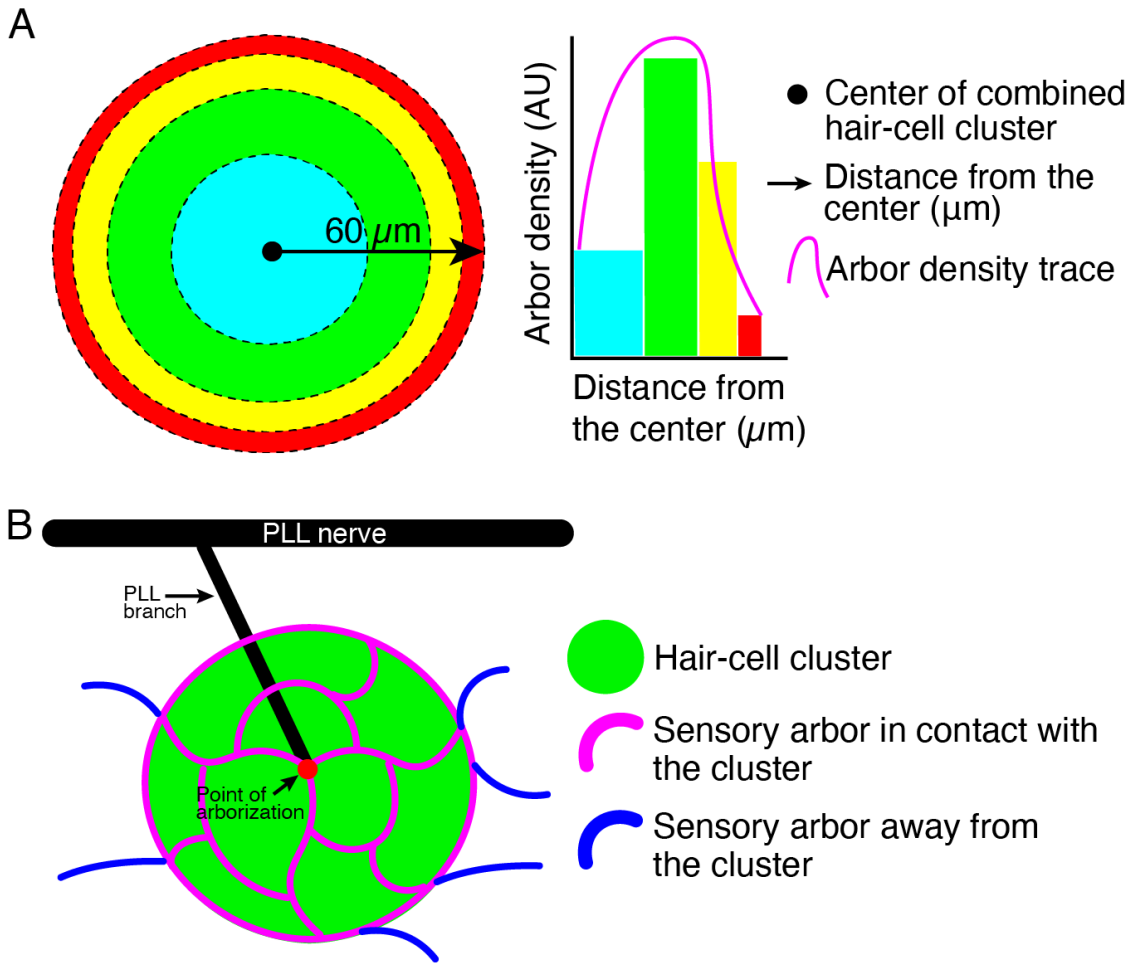

Figure 2—figure supplement 2. Quantification of sensory arbor distributions and contacts with hair cell clusters. (A) A schematic drawing of the combined hair cell cluster and surrounding region depicts concentric sections of equal area in distinct colors (cyan, green, yellow, and red). The arbor density is plotted as a histogram against the distance (black arrow) from the center (black circle) of the combined hair cell cluster. The histogram is represented as a density trace graph (magenta). (B) A schematic drawing of a posterior lateral-line neuromast depicts the posterior lateral-line (PLL) nerve (black), posterior lateral-line branch (black), the point or arborization, the sensory arbors (magenta) that contact the hair cell cluster (green), and the sensory arbors that project away (blue) from the hair cell cluster.

1046 **Videos 2 and 3. FM4-64 labels the hair cells of both control and *sema7a*$^{-/-}$ mutant**
1047 **neuromasts**. Through-focus scans of 4 dpf control (Video 2) and *sema7a*$^{-/-}$ mutant (Video 3)
1048 neuromasts depict the hair cells (green) that have incorporated FM4-64. The sensory arbors
1049 (magenta) are tightly associated with the clustered hair cells in the control neuromast but show
1050 aberrant arborization in the *sema7a*$^{-/-}$ larvae.

1051 **Video 4. Three-dimensional arborization patterns in control and *sema7a*$^{-/-}$ neuromasts.**
1052 Lateral views depict **t**hree-dimensionally rendered combined skeletonized network traces from
1053 27 control and 27 *sema7a*$^{-/-}$ mutant neuromasts at 4 dpf.
1054

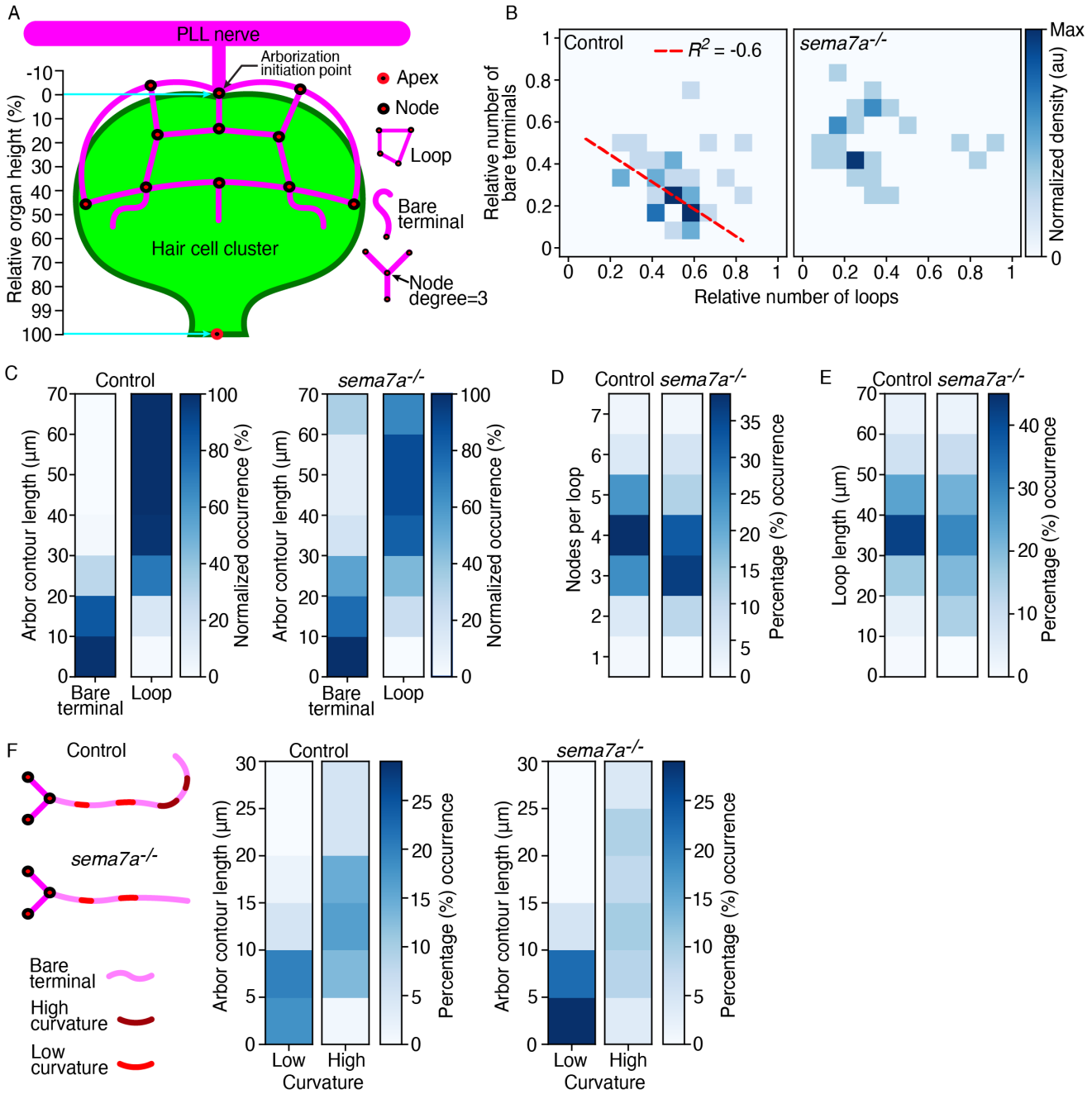

Figure 3. Sema7A patterns the topology of the sensory arbor network. (A) A schematic drawing of the combined hair cell cluster (green) and associated sensory axons (magenta) shows diverse topological features of the arborization network, including nodes, loops, bare terminals, node degree, and bare-terminal curvature. The apex is defined as the center of the hair bundle cluster and the base is denoted by the node from which the arborizations extends. The relative organ height describes the position along the axis formed between the arborization

1061 initiation point and the apex of the hair cell cluster. (B) The correlation between the relative
1062 number of bare terminals and loops from 35 control neuromasts and 27 *sema7a*$^{-/-}$ neuromasts
1063 at 4 dpf shows a negative correlation in the control but a scattered distribution in the mutants.
1064 The same neuromasts were analyzed in the subsequent panels. R^2, correlation coefficient.
1065 Dashed red line depicts the regression slope. (C) The relationship of contour lengths to bare
1066 terminals and loops reveals reduced looping in the mutants. (D) Quantification of the number
1067 of nodes per loop demonstrates a decrease in mutants. (E) Mutant larvae manifest a broader
1068 distribution of loop lengths compared to controls. (F) A schematic diagram of the extending
1069 bare terminals depicts regions of high and low curvature along the length of the arbor. The
1070 distributions of bare terminals between low- and high-curvature groups show an enrichment of
1071 long, highly curved arbors in the control and short, linear arbors in the mutants. Statistical
1072 analyses are displayed in Table 1.
1073

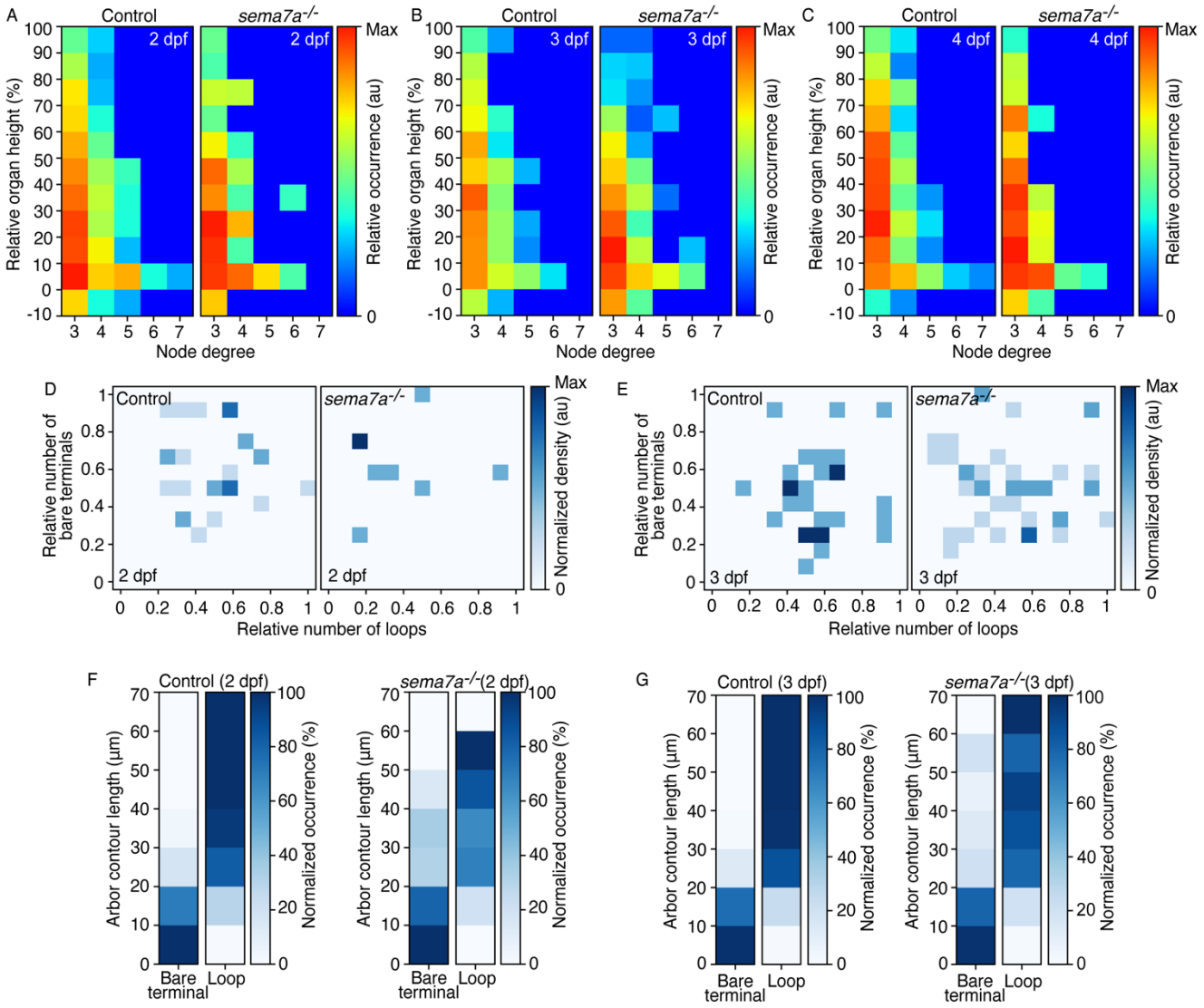

Figure 3—figure supplement 1. Quantification of topological features across developmental stages and genotypes. (A-C) The distribution of node degrees as a function of the height in hair cell clusters shows the difference in the network's hierarchical organization between control and *sema7a*$^{-/-}$ larvae. Nodes of low degree are commonly observed between genotypes across developmental stages (A, B), but their distribution along the cluster height became significantly different at 4 dpf (C), with nodes in control larvae localizing higher along the axis than in the mutants. In this and the following two panels, 33, 29, and 35 neuromasts were analyzed from 2 dpf, 3 dpf, and 4 dpf control larvae, respectively and 17, 53, and 27 neuromasts were analyzed from 2 dpf, 3 dpf, and 4 dpf *sema7a*$^{-/-}$ mutant larvae, respectively (D, E) The correlations between the relative number of bare terminals and loops from control

1084 and *sema7a*$^{-/-}$ neuromasts reveal dispersive distributions at both 2 dpf (D) and 3 dpf (E) stages,
1085 suggesting that the networks are undergoing reorganization and yet to adopt an ordered
1086 topology. (F,G) In the distribution of arbors between bare terminals and loops with respect to
1087 their contour lengths, mutants' arbors display significantly higher propensity to remain as bare
1088 terminals compared to the controls at both 2 dpf (F) and 3 dpf (G). The samples were identical
1089 to those in the previous panel. Statistical analyses are displayed in Table 1.
1090

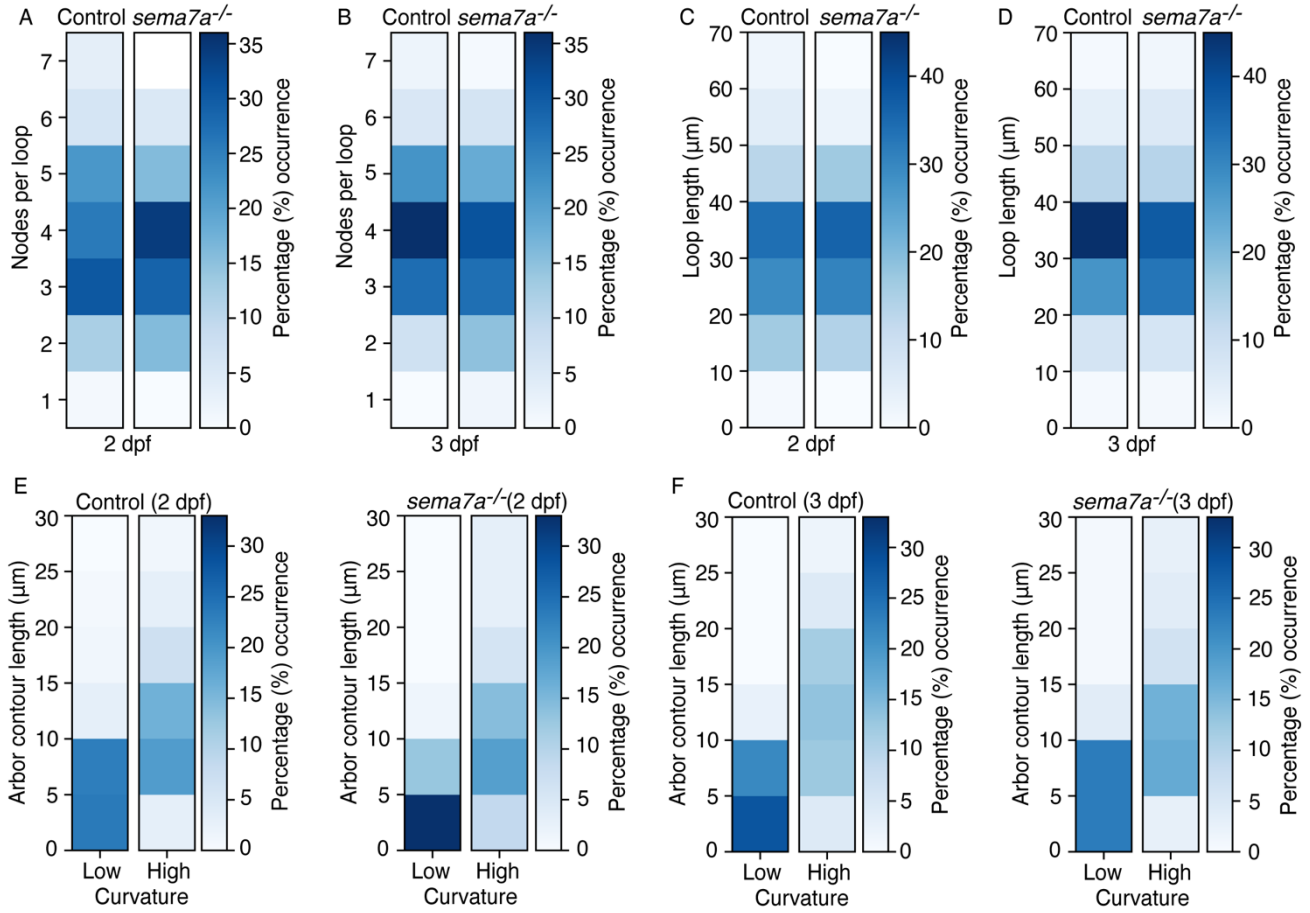

Figure 3—figure supplement 2. Quantification of topological features between control and *sema7a*$^{-/-}$ larvae across developmental stages. (A, B) Quantifications of the number of nodes per loop demonstrate a broader, but not significantly different, distribution in the mutants than the controls at both 2 dpf (A) and 3 dpf (B). In this and the following panels, 33 and 29 neuromasts were analyzed from 2 dpf and 3 dpf control larvae, respectively and 17 and 53 neuromasts were analyzed from 2 dpf and 3 dpf *sema7a*$^{-/-}$ mutant larvae, respectively. (C, D) Quantifications of loop lengths from the same larvae indicate a wider, but not significantly different, distribution in the mutants than the controls at both 2 dpf (C) and 3 dpf (D). (E, F) The distributions of bare terminals between low- and high-curvature groups from the same larvae show higher occurrences of long, curved arbors in the control and short, linear arbors in the mutants at both 2 dpf (E) and 3 dpf (F) stages. Statistical analyses are displayed in Table 1.

Height of node degrees	*p*-values (control vs *sema7a*$^{-/-}$)		
	2 dpf	3 dpf	4 dpf
Degree = 3	3.50E-01	1.05E-08***	1.68E-03**
Degree = 4	3.85E-01	7.11E-02	1.71E-03**
Degree = 5	4.60E-01	5.23E-01	4.40E-01
Bare terminals vs Loop	2 dpf	3 dpf	4 dpf
0 to 10 μm	3.84E-01	7.89E-01	2.11E-01
10 to 20 μm	3.50E-02*	3.92E-01	2.94E-02*
20 to 30 μm	2.28E-04***	2.63E-02*	3.82E-09***
30 to 40 μm	5.04E-59***	3.63E-25***	1.28E-33***
40 to 70 μm	———	———	———
Nodes per loop	5.06E-01	1.96E-01	3.50E-02*
Loop length	5.81E-01	2.71E-01	2.21E-02*
Distribution of bare terminal curvature	2 dpf	3 dpf	4 dpf
	4.23E-01	8.91E-01	1.99E-02*

Table 1. Statistical comparison between control and *sema7a*$^{-/-}$ larvae for topological features. One-sided Kolmogorov-Smirnov tests were used to assess the difference in node degree heights, nodes per loop, and loop lengths for control *versus sema7a*$^{-/-}$ neuromasts at 2 dpf, 3 dpf, and 4 dpf. In each of these cases, the difference in the distributions were not significantly different (*p*-values in red) between the control and the mutants at 2 dpf and 3 dpf but became significantly different (*p*-values in green) at 4 dpf. Chi-square tests were used to assess the difference in occurrences of bare terminals versus loops, as well as the occurrences of bare terminals with low versus high curvature. The distribution at 4 dpf shows significant difference between the control and the mutant larvae. The occurrence of significant differences at 4 dpf for diverse topological features suggest that Sema7A function is required to achieve an ordered network topology at a mature stage. Thirty-three, 29, and 35 neuromasts were

1115 analyzed from 2 dpf, 3 dpf, and 4 dpf control larvae, respectively, and 17, 53, and 27
1116 neuromasts were analyzed from 2 dpf, 3 dpf, and 4 dpf *sema7a*$^{-/-}$ mutant larvae, respectively.
1117 * Signifies $p < 0.05$, ** signifies $p < 0.01$, and *** signifies $p < 0.001$.
1118

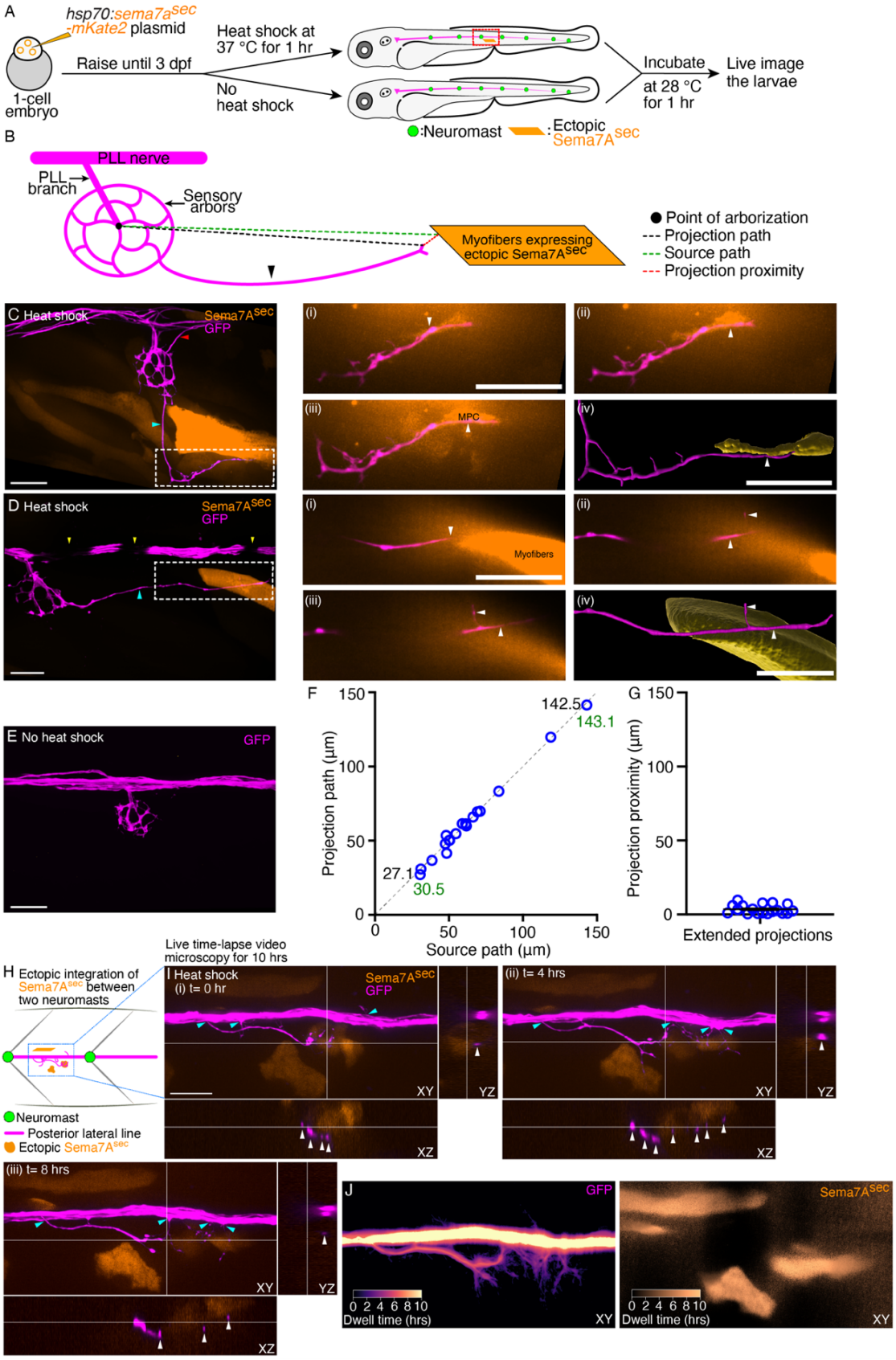

1119 **Figure 4. Ectopic Sema7A^sec diffusive cue provides neural guidance *in vivo*.** (A) A

1120 diagrammatic overview depicts the generation of a transgenic animal that expresses the
1121 Sema7A^{sec} protein ectopically under the control of a thermally inducible promoter. Larvae with
1122 ectopic myotomal-integration near the network of sensory arbors (red rectangle) were imaged
1123 to analyze arbor morphology. (B) A schematic drawing of a sensory arbor from a heat-shocked
1124 larva depicts an extended axonal projection (arrowhead) that reaches toward the myofibers
1125 expressing the ectopic Sema7A^{sec} protein. Parameters that quantitate the accuracy of the
1126 extended axonal projections toward the ectopic Sema7A^{sec} sources are denoted. (C) In a
1127 micrograph of an ectopically expressing Sema7A^{sec} (orange) larva, the sensory arbor
1128 (magenta) extends two aberrant axonal projections. One elongates (cyan arrowhead) along
1129 the somite boundary to reach and contact an ectopically integrated muscle progenitor cell
1130 (white dashed line) and the other (red arrowhead) reenters the posterior lateral-line nerve while
1131 following a second ectopic source. The through-focus scans (i–iii) from the epidermis to the
1132 dermomyotome and the three-dimensional (3D) surface reconstruction (iv) reveal the intimate
1133 contact between the aberrant sensory arbor (arrowheads) and the muscle progenitor cell. (D) In
1134 a micrograph of an ectopically expressing Sema7A^{sec} (orange) larva, the sensory arbor
1135 (magenta) extends a single aberrant axonal process (cyan arrowhead) to reach ectopically
1136 integrated myofibers (white dashed line). The through-focus scans (i–iii) from the epidermis to
1137 the dermomyotome and the 3D surface reconstruction (iv) reveal the proximal association of
1138 the aberrant sensory arbor (arrowheads) to the myofibers. Melanocytes (yellow arrowhead)
1139 along the horizontal myoseptum intermittently block the visibility of the lateral-line nerve. (E) An
1140 injected, but not heat-shocked, control larva does not express ectopic Sema7A^{sec} and does not
1141 show aberrant projection from the sensory arbor. (F) A plot demonstrates the accuracy of 18
1142 extended axonal arbors in finding ectopic Sema7A^{sec} sources. Each circle represents a single
1143 ectopic integration event. The two pairs of numbers represent the minimal and maximal lengths
1144 of the projection path (black) and its corresponding source path (green). (G) A plot quantitates
1145 the distribution of projection-proximity length from 18 ectopic integration events. (H) A
1146 schematic drawing of a section of the lateral-line nerve between two neuromasts from a heat-
1147 shocked larva depicts a few extended neurites (magenta) reaching toward the cells expressing

1148 the ectopic Sema7A^{sec} protein (orange). The Sema7A^{sec} integration site (blue rectangle) with
1149 the sensory axonal projections was imaged for ten hours to visualize axonal dynamics. (I)
1150 Micrographs (i-iii) at three distinct times in the time-lapse video microscopy show directed
1151 branching (cyan arrowheads) of the sensory neurites from the lateral-line nerve toward the
1152 ectopic Sema7A^{sec} sources. Each panel depicts the ectopic integration site and the associated
1153 sensory neurites from three different planes, XY, XZ, and YZ. White arrowheads in XZ and YZ
1154 planes highlight the close association of the sensory axons with the ectopic Sema7A^{sec}
1155 sources. The t=0 hr denotes the onset of imaging, which is two hours post the beginning of
1156 heat shock. (J) The micrographs depict in pseudocolored trajectories the dwell times of the
1157 sensory neurites (left) at the Sema7A^{sec} sources (right) for ten hours. MPC, muscle progenitor
1158 cell; scale bars, 20 μm; means ± SEMs.
1159

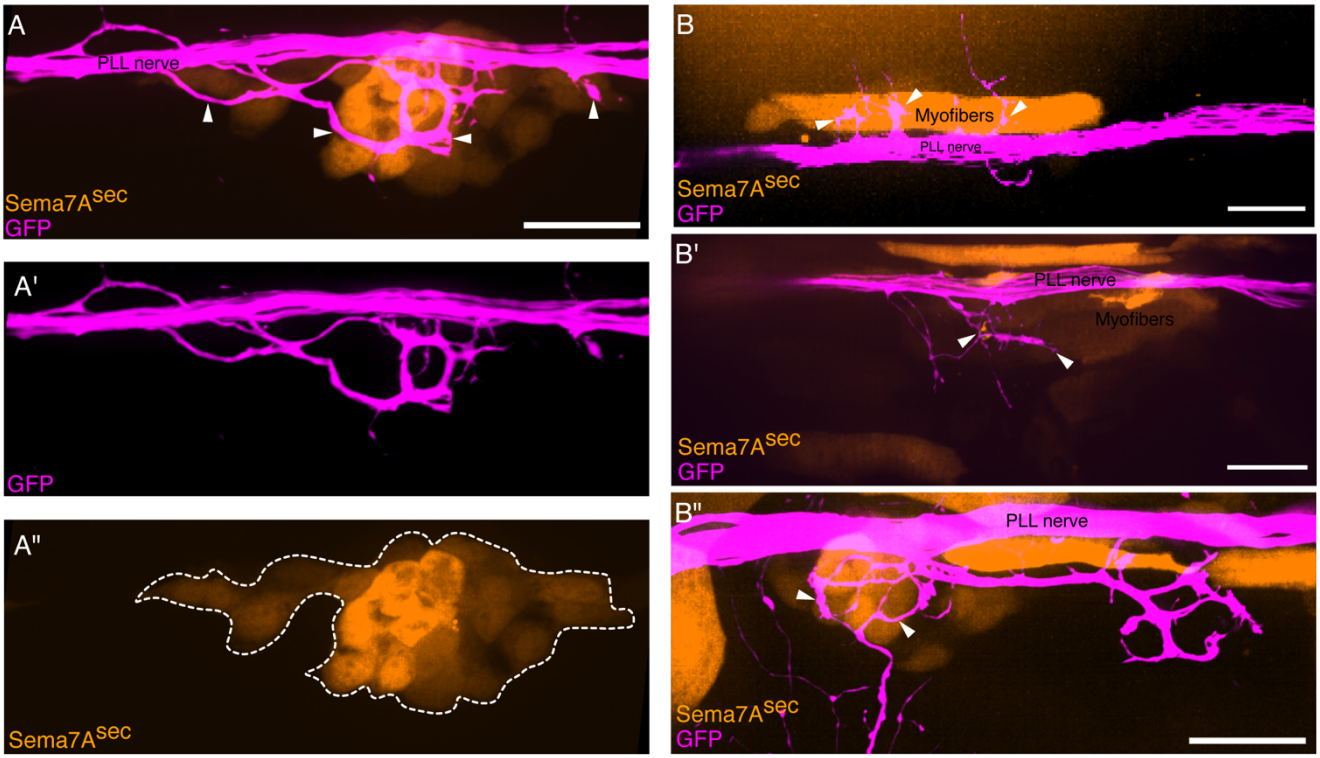

1160 **Figure 4—figure supplement 1. Ectopic Sema7A^{sec} diffusive cues induce aberrant**
1161 **sensory neurite extension.** (A-A") In a micrograph of an ectopically expressing Sema7A^{sec}
1162 (orange) larva, the sensory arbors (magenta) extend multiple axonal projections (arrowheads)
1163 that reenter the lateral-line nerve while following an ectopic Sema7A source. Maximal-intensity
1164 projections of the sensory arbors and the ectopically expressing Sema7A cells (white dashed
1165 line) are shown in A' and A", respectively. (B-B") Micrographs depict three individual incidents
1166 of ectopic *sema7a^{sec}* (orange) integrations that occurred distant from neuromasts. In each
1167 case, a set of myofibers expresses the ectopic Sema7A^{sec} protein that induces neurite
1168 extensions (arrowheads) from the lateral-line nerve (magenta) toward itself. Scale bars, 20 μm.
1169

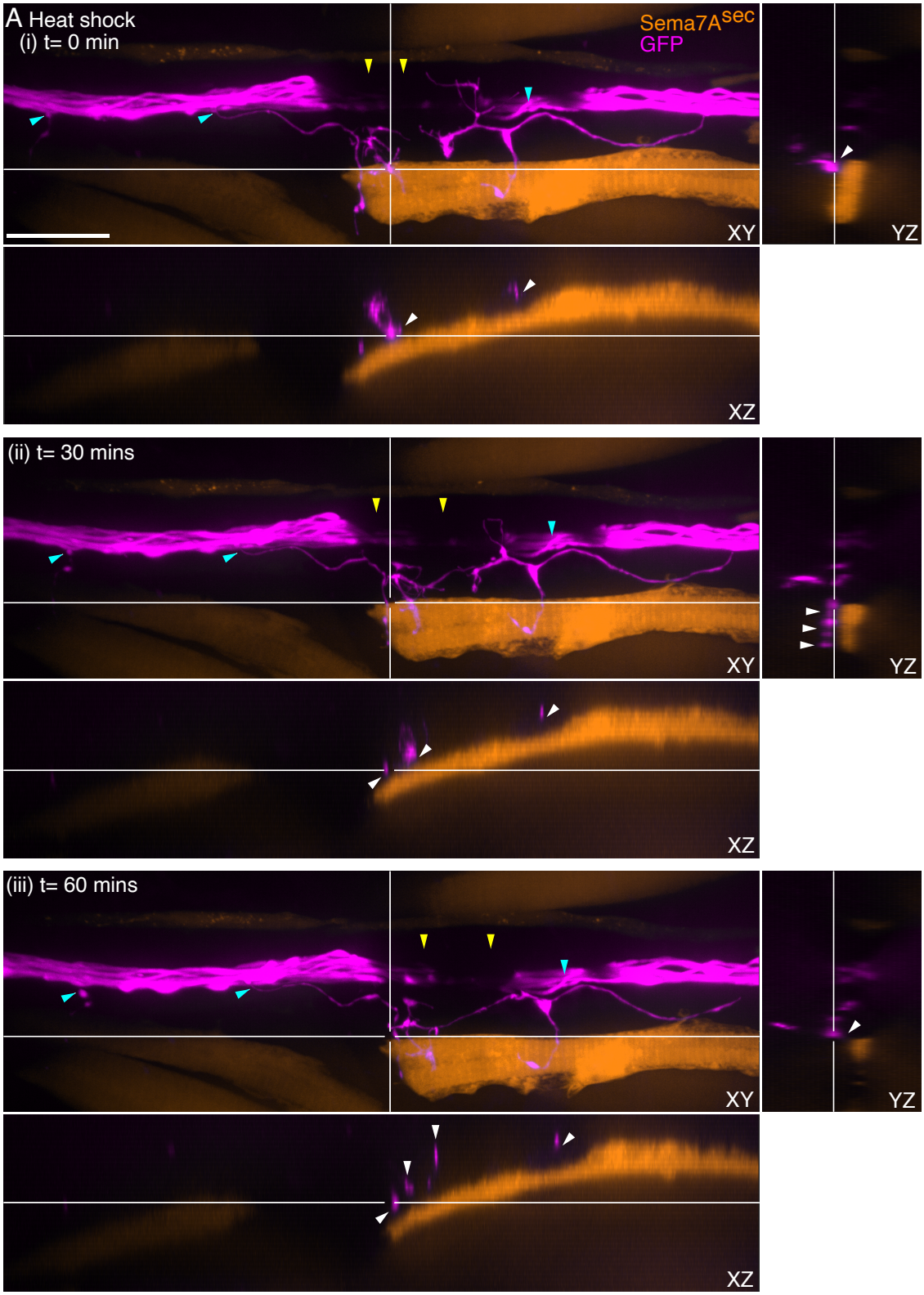

1170

1171 **Figure 4—figure supplement 2. Ectopic integration of Sema7A^{sec} distant from the**
1172 **neuromast induces sensory neurite extension.** (A) Micrographs of a section of the lateral-
1173 line nerve between two neuromasts from a 3-dpf heat-shocked larva depicts a few extended
1174 neurites (magenta) reaching toward the cells expressing the ectopic Sema7A^{sec} (orange). The

1175 Sema7A^{sec} integration site with the sensory axonal projections was imaged for one hour to
1176 visualize axonal dynamics. Micrographs (i-iii) at three distinct time-points from the time-lapse
1177 video microscopy show directed branching (cyan arrowheads) of the sensory neurites from the
1178 lateral-line nerve toward the ectopic Sema7A^{sec} sources. Each panel depicts the ectopic
1179 integration site and the associated sensory neurites from three different planes, XY, XZ, and
1180 YZ. White arrowheads in XZ and YZ planes highlight the close association of the sensory axons
1181 with the ectopic Sema7A^{sec} sources. Melanocytes (yellow arrowheads) along the horizontal
1182 myoseptum intermittently block the visibility of the lateral-line nerve. Scale bar, 20 μm.
1183

1184 **Video 5. Sensory axonal projections contact an embryonic muscle progenitor cell**
1185 **expressing Sema7A^{sec}.** A through-focus scan of a 3 dpf larva depicts a muscle progenitor
1186 cell in the dermomyotome that expresses the ectopic Sema7A^{sec} (orange) and the sensory
1187 axonal projection (magenta) that makes intimate contact with it. Scale bar, 20 μm.

1188 **Video 6. Volumetric surface reconstruction of a sensory arbor and an embryonic muscle**
1189 **progenitor expressing Sema7A^{sec}.** Reconstruction of the muscle progenitor cell (orange) at
1190 3 dpf reveals its intimate association with an attracted sensory arbor (magenta).

1191 **Video 7. Volumetric surface reconstruction of a sensory arbor and the mature myofibers**
1192 **expressing Sema7A^{sec}.** Reconstruction of mature myofibers expressing ectopic Sema7A^{sec}
1193 (orange) at 3 dpf shows their close association with the attracted sensory arbors (magenta).

1194 **Video 8. Sensory axonal projections remain in proximity to myofibers expressing**
1195 **Sema7A^{sec}.** A through-focus scan of a 3 dpf larva depicts mature myofibers expressing
1196 exogenous Sema7A^{sec} deep in the myotome (orange) and the sensory axonal projection
1197 (magenta) that remains nearby.

1198 **Video 9. Aberrant axonal projections reenter the lateral-line nerve while following an**
1199 **ectopic Sema7A^{sec} source.** A through-focus scan of a 3 dpf larva depicts cells expressing
1200 exogenous Sema7A^{sec} (orange) that guides the aberrant sensory axonal projection (magenta)
1201 back into the lateral-line nerve. Scale bar, 20 μm.

1202 **Videos 10, 11, and 12. Ectopic Sema7A^{sec} expression induces aberrant neurite**
1203 **projections from the lateral-line nerve.** Through-focus scans of 3 dpf larvae depict three
1204 individual incidents of ectopic *sema7a^{sec}* (orange) integrations that occurred distant from the
1205 neuromasts. In each case, myofibers express ectopic Sema7A^{sec} protein (orange) that attracts
1206 neurite extensions from the lateral-line nerve (magenta). Scale bars, 20 μm.

1207 **Videos 13 and 14. Volumetric reconstructions depict close contacts between the**
1208 **sensory neurites and the ectopic Sema7a^{sec} expressing cells.** Volumetric reconstructions
1209 of 3 dpf larvae depict two individual incidents of ectopic *sema7a^{sec}* (orange) integrations that
1210 occurred distant from the neuromasts. In each case, myofibers or random mosaic of cells in
1211 the dermomyotome express ectopic Sema7A^{sec} protein (orange) that attracts neurite
1212 extensions from the lateral-line nerve (magenta).

1213 **Video 15 and 16. Time-lapse video microscopies depict the dynamics between the**
1214 **sensory neurites and the ectopic Sema7a^{sec} expressing cells.** Time-lapse images of 3 dpf
1215 larvae depict two individual incidents where the ectopic Sema7A^{sec} sources (orange) induce
1216 directed branching of the sensory neurites (magenta) from the lateral-line nerve toward itself.
1217 Within each time-lapse videos, individual panel depicts the ectopic integration site and the
1218 associated sensory neurites from three different planes, XY, XZ, and YZ. Scale bars, 20 μm.
1219

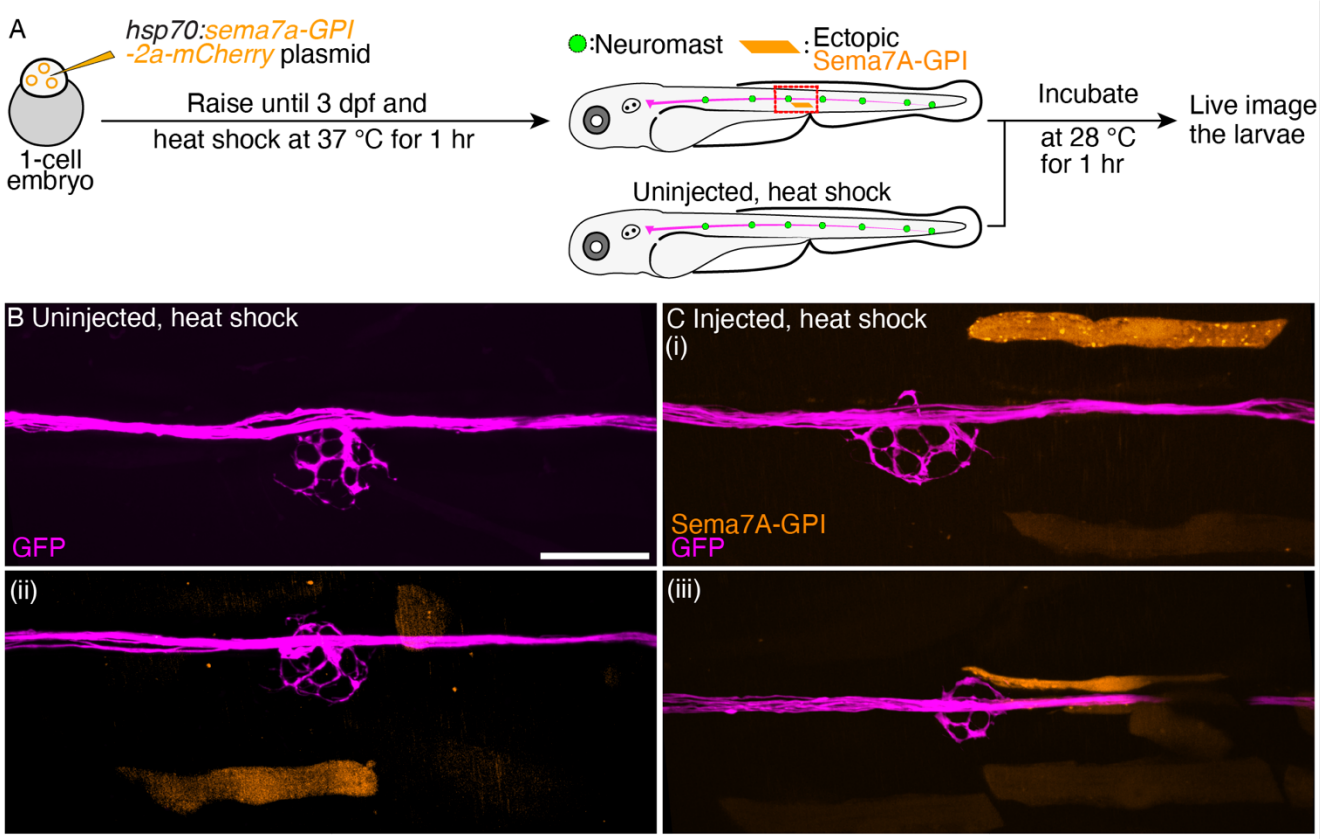

Figure 5. Ectopic Sema7A-GPI fails to guide sensory arbors from a distance. (A) A diagrammatic overview depicts the generation of a transgenic animal that expresses the Sema7A-GPI protein ectopically under the control of a thermally inducible promoter. Larvae with ectopic myotomal-integration near the network of sensory arbors (red rectangle) were imaged to analyze arbor morphology. Uninjected, heat-shocked larvae were used as controls. (B) Uninjected and heat-shocked larva depicts normal arborization pattern of the sensory axons (magenta). (C) Injected and heat-shocked larvae robustly express the Sema7A-GPI in the myofibers (orange). Panels (i-iii) depict the ectopically expressing Sema7A-GPI myofibers that fail to attract sensory arbors toward itself. Scale bar, 20 μm.

1230 **Videos 17, 18, and 19. Sema7A-GPI is incapable to impart sensory axon guidance from**
1231 **a distance.** Through-focus scans of 3 dpf larvae depict three individual incidents of ectopic
1232 *sema7a-GPI* integrations that occurred near the sensory arbor network. In each case,
1233 myofibers robustly express ectopic Sema7A-GPI protein (orange) but the sensory arborization
1234 pattern (magenta) remain unperturbed. Scale bars, 20 μm.
1235

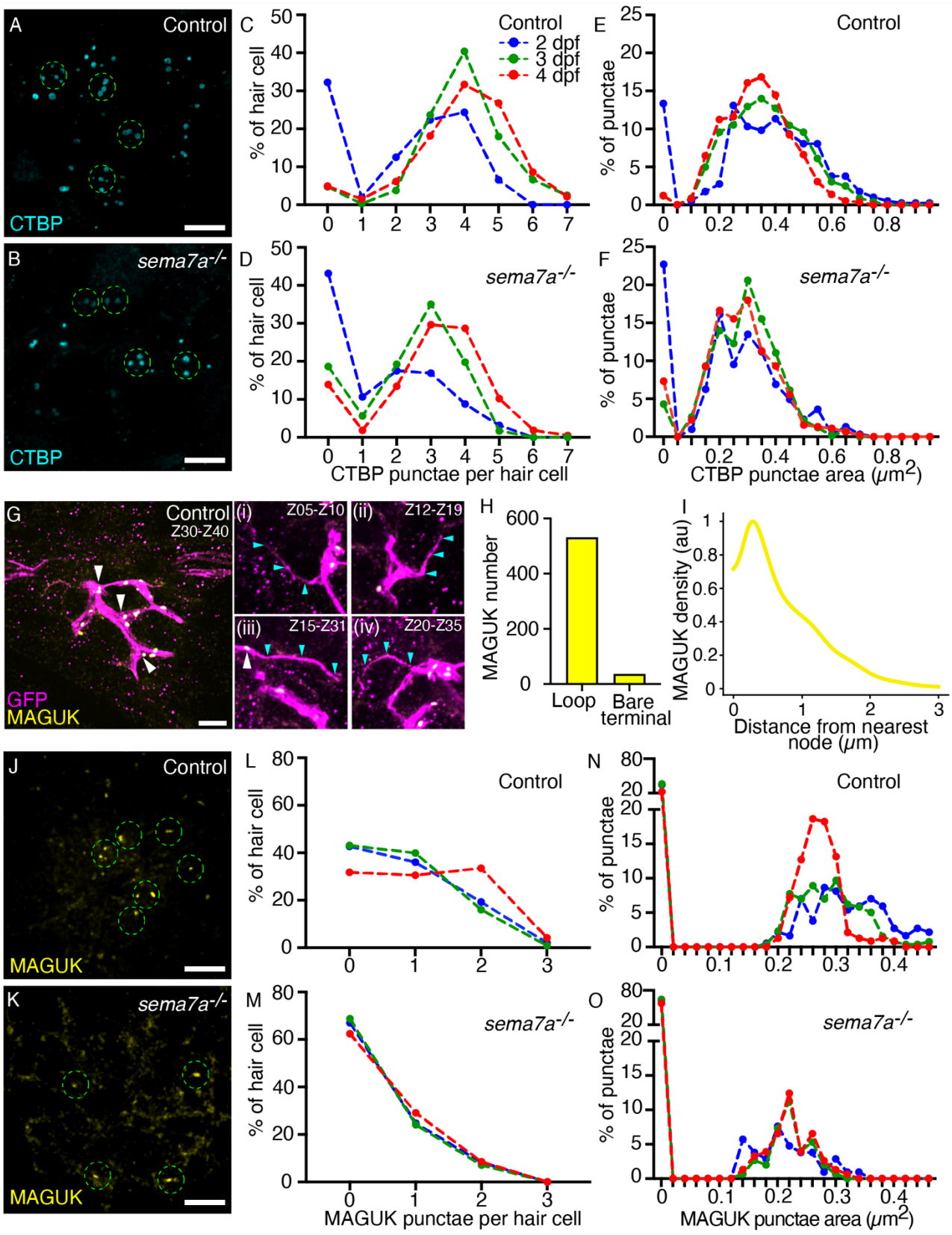

Figure 6. Sema7A deficiency impairs synaptic assembly. (A,B) Maximal-intensity projections of micrographs from a control and a *sema7a*$^{-/-}$ neuromast depict the presynaptic

1238 aggregates marked by CTBP (cyan). The approximate hair cell basal region is outlined by
1239 dashed green circles. (C-F) Plots quantitate the numbers of presynaptic aggregates (C,D) and
1240 their areas (E,F), in each hair cell across developmental stages. One hundred and fifty-two,
1241 317, and 325 hair cells were analyzed from 2 dpf, 3 dpf, and 4 dpf control larvae, respectively.
1242 One hundred and sixty, 216, and 177 hair cells were analyzed from 2 dpf, 3 dpf, and 4 dpf
1243 *sema7a*$^{-/-}$ mutant larvae, respectively. (G) A micrograph generated from maximal-intensity
1244 projection of ten consecutive through-focus scans across Z-planes of a control 4 dpf neuromast
1245 depict the sensory arbors (magenta) and the postsynaptic aggregates marked by MAGUK
1246 (yellow, white arrowheads). The MAGUK punctae primarily occur on the loop and aggregate
1247 near the nodes. Panels (i-iv) depict maximal-intensity projection of consecutive through-focus
1248 scans of distinct Z-planes to show bare terminals. In each panel, the bare terminal (magenta,
1249 cyan arrowheads) rarely harbors postsynaptic aggregates (yellow, white arrowhead). (H)
1250 Quantification of the distribution of the MAGUK-punctae between the two topological features
1251 of the network depicts enrichment of postsynaptic densities on the loops over the bare
1252 terminals. (I) A histogram shows the distribution of MAGUK-punctae density against the
1253 distance from the node. The histogram is represented as a density trace graph (yellow). For
1254 both H and I, five hundred and sixty-seven MAGUK punctae were analyzed from 16
1255 neuromasts of 4 dpf larvae. (J,K) Maximal-intensity projections from micrographs of a control
1256 and a *sema7a*$^{-/-}$ neuromast depict the postsynaptic aggregates marked by MAGUK (yellow).
1257 The approximate hair cell basal region is outlined by dashed green circles. (L-O) Plots
1258 quantitate the numbers of postsynaptic aggregates (L,M) and their areas (N,O), in each hair
1259 cell across developmental stages. One hundred and fifty, 218, and 167 hair cells were analyzed
1260 from 2 dpf, 3 dpf, and 4 dpf control larvae, respectively. Ninety-seven, 141, and 141 hair cells
1261 were analyzed from 2 dpf, 3 dpf, and 4 dpf *sema7a*$^{-/-}$ mutant larvae, respectively. Scale bars,
1262 5 μm.
1263

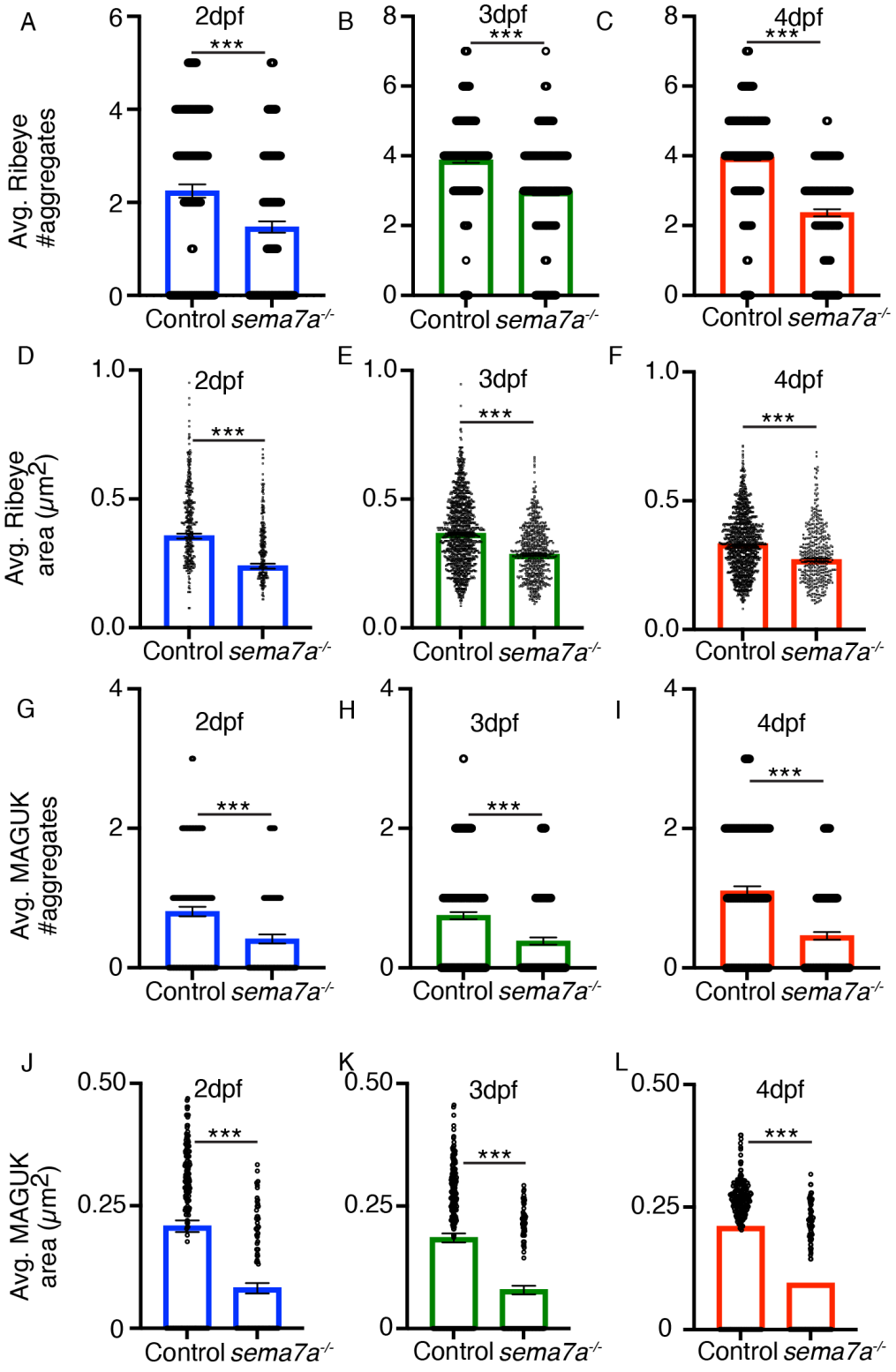

Figure 6—figure supplement 1. *sema7a*$^{-/-}$ mutants display impaired synaptic assembly. (A-F) The plots quantitate the average numbers and areas of presynaptic aggregates from control and *sema7a*$^{-/-}$ neuromasts. Significant decreases in the numbers and areas of

presynaptic aggregates are observed across development. Three hundred and forty-one, 1229, and 1286 presynaptic aggregates were analyzed from 2 dpf, 3 dpf, and 4 dpf control larvae, respectively. Two hundred and thirty-five, 643, and 419 presynaptic aggregates were analyzed from 2 dpf, 3 dpf, and 4 dpf *sema7a*$^{-/-}$ mutant larvae, respectively. (G-L) The plots quantitate the average numbers and areas of postsynaptic aggregates from control and *sema7a*$^{-/-}$ neuromasts. Significant decreases in the numbers and areas of postsynaptic aggregates occurred during development. Three hundred and ninety-seven, 1243, and 1300 postsynaptic aggregates were analyzed from 2 dpf, 3 dpf, and 4 dpf control larvae, respectively. Three hundred and four, 651, and 451 postsynaptic aggregates were analyzed from 2 dpf, 3 dpf, and 4 dpf *sema7a*$^{-/-}$ mutant larvae, respectively. Means ± SEMs; *** implies $p < 0.001$.

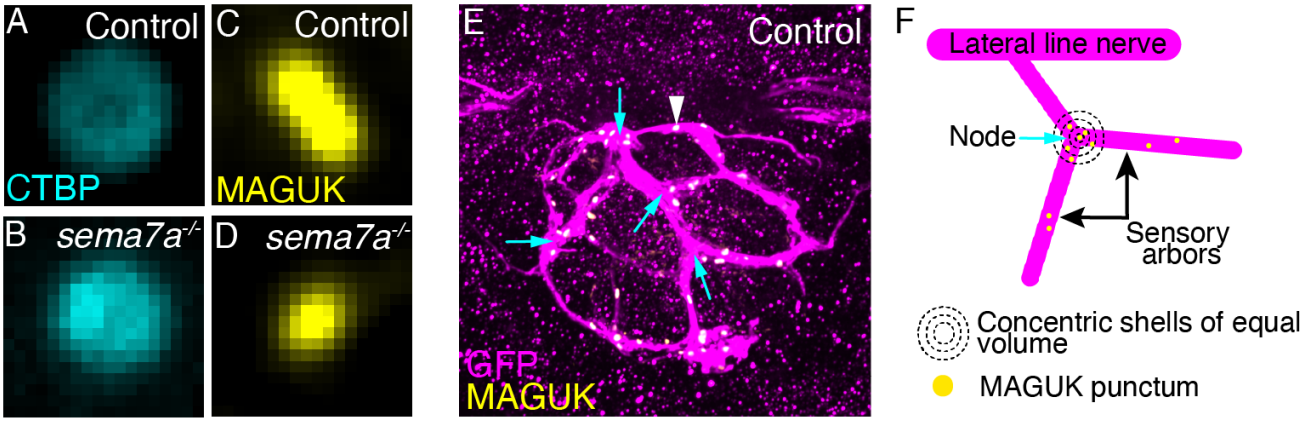

Figure 6—figure supplement 2. Morphologies of presynaptic and postsynaptic assemblies and the distribution of postsynaptic aggregates across the sensory arbor network. (A,B) The micrographs depict single presynaptic aggregate marked by CTBP in control (A) and in sema7a-/- mutant (B) larvae at 4 dpf. (C,D) The micrographs depict single postsynaptic aggregate marked by MAGUK in control (C) and in sema7a-/- mutant (D) larvae at 4 dpf. (E) A maximal-intensity projection micrograph depicts the sensory arbor network (magenta) and the enrichment of the postsynaptic assemblies (yellow, white arrowhead) near the nodes (cyan arrows). (F) A schematic diagram of the sensory arbor network depicts the enrichment of the MAGUK punctae near the node (cyan arrow). The three-dimensional space surrounding each node was divided into concentric shells of equal volume to measure the distribution of MAGUK-punctae density across the network.

1315 **Video 20. Postsynaptic assemblies are enriched in the loops and near the nodes of a**
1316 **sensory arbor network.** Through-focus scans of a 4 dpf neuromast depict the sensory arbor
1317 network (magenta) where the postsynaptic assemblies (yellow) are primarily located in the
1318 loops of the arbor network and are enriched near the nodes.
1319

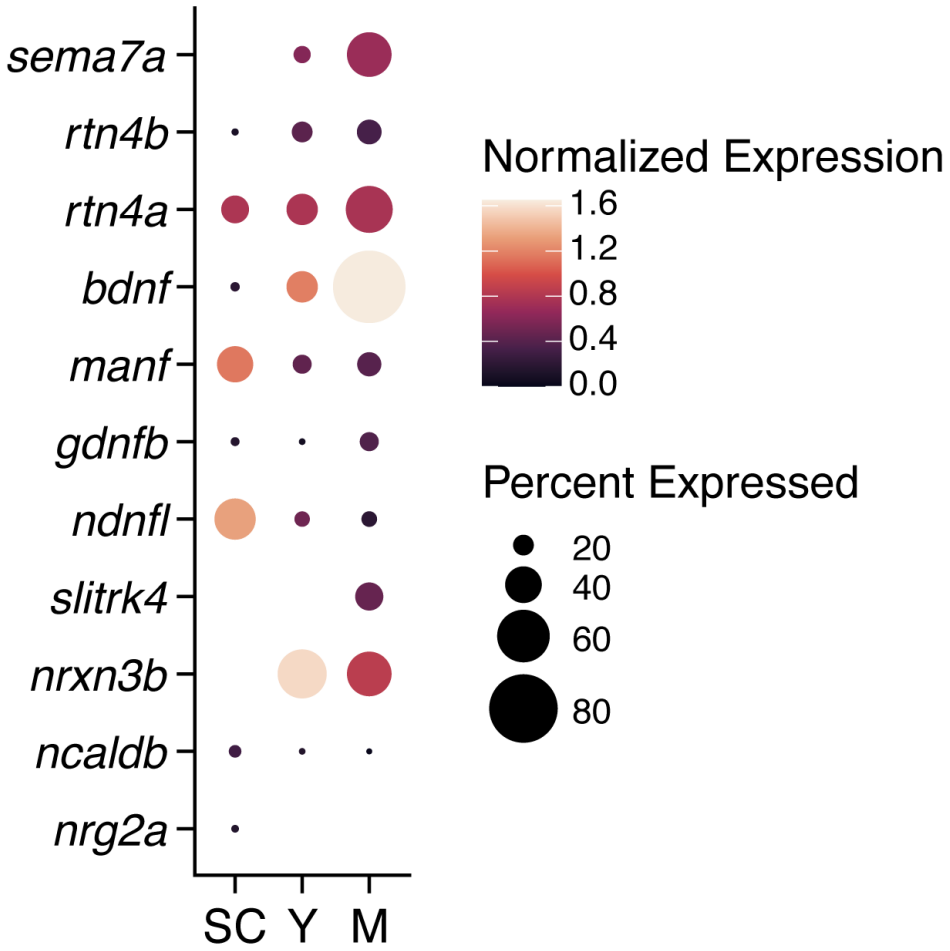

Figure 7. Expression of diverse neural guidance cues in developing neuromasts. Analysis of single cell RNA-sequencing data (9) shows the expression of multiple neural guidance genes that are expressed across young hair cells (Y), mature hair cells (M), and support cells (SC). Dot sizes and colors signify the proportion of cells in each cluster that express a gene and the average strength of expression (log[(counts/10,000) +1]), respectively.